Vaz-Romero, A.; Rodríguez-Martínez, J. A.; Mercier, S.; Molinari, A. Multiple necking pattern in nonlinear elastic bars subjected to dynamic stretching: the role of defects and inertia. *International Journal of Solids and Structures,* Vol. 125, Pp. 232-243, 15 March 2017

DOI: https://doi.org/10.1016/j.ijsolstr.2017.07.001

Multiple necking pattern in nonlinear elastic bars subjected to dynamic stretching: The role of defects and inertia

A. Vaz-Romero[a], J. A. Rodríguez-Martínez[a,b], S. Mercier[b], A. Molinari[b,*]

[a]*Department of Continuum Mechanics and Structural Analysis. University Carlos III of Madrid. Avda. de la Universidad, 30. 28911 Leganés, Madrid, Spain*
[b]*Laboratoire d'Etudes des Microstructures et de Mécanique des Matériaux LEM3, UMR CNRS 7239, Université de Lorraine, Ile du Saulcy, 57045 Metz cedex 1, France*

Abstract

In this paper we explore the inception and development of multiple necks in incompressible nonlinear elastic bars subjected to dynamic stretching. The goal is to elucidate the role played by a spatial-localized defect of the strain rate field in the necking pattern that emerges in the bars at large strains. For that task, we have used two different approaches: (1) finite element simulations and (2) linear stability analyses. The finite element simulations have revealed that, while the defect of the strain rate field speeds up the development of the necking pattern in the late stages of the localization process, the characteristic (average) neck spacing is largely independent of the defect within a wide range of defect amplitudes. The numerical results have been rationalized with the linear stability analyses, which enabled to explain the average spacing characterizing the necking pattern at high strain rates. Moreover, the numerical calculations have also shown that, due to inertia effects, the core of the localization process occurs during the post-uniform deformation regime of the bar, at strains larger than the one based on the Considère criterion. This phenomenon of neck retardation is shown to have a meaningful influence on the necking pattern.

Keywords:
Dynamic necking, Nonlinear elasticity, Linear stability analysis, Numerical calculations, Inertia

---

1. Introduction

The problems of flow localization and fragmentation in ductile solids subjected to high loading rates have been intensively investigated over the last 70 years. This research field, which has been traditionally pushed forward by the aerospace and defence industries, is now especially active and

---

[*] Corresponding author. Tel. +33 387315369; Fax: +33 387315366. E-mail address: alain.molinari@univ-lorraine.fr

challenging due to the increasing requirements to improve the protection of vehicles, aircraft and critical infrastructures from attacks and man-made or natural disasters. A review on the recent scientific literature enlightens the significant number of papers that have been published in this specific topic over the last decade (Zhang and Ravi-Chandar, 2006; Zhou et al., 2006; Rusinek and Zaera, 2007; Lindgreen et al., 2008; Zhang and Ravi-Chandar, 2010; Mercier et al., 2010; Janiszewski, 2012; Rodríguez-Martínez et al., 2013a; Dequiedt, 2015; Ravi-Chandar and Triantafyllidis, 2015). Most of the cited works were focused on the dynamic radial expansion of rings (Niordson, 1965). The principal advantage of the rapidly expanding ring test is that, due to the symmetry of the problem, the effects of wave propagation are nearly eliminated before flow localization occurs in the form of multiple necks which ultimately lead to the fragmentation of the sample (Hu and Daehn, 1996). All the published works (either analytical, numerical or experimental) agree that, for ductile materials, the number of necks nucleated in the sample and the number of fragments increase with the applied loading rate. Furthermore, it has been shown that the proportion of necks that develop into fracture sites also increases as the loading rate increases (Rodríguez-Martínez et al., 2013a). Nevertheless, the aetiology of such phenomena is still today a source of debate in the Solid Mechanics community. It clearly exists a lack of agreement on the mechanisms which control the necking and fragmentation patterns.

Multiple necking and fragmentation have been classically modelled with statistical approaches which establish a direct connection between (material, geometrical ...) defects, nucleated necks and fracture sites. The pioneering work of Mott (1947) set the basis for the statistical theory which has been further developed, for instance, by Grady and co-workers (Grady, 1981; Kipp and Grady, 1985; Grady and Olsen, 2003) and Dequiedt (2015). The formation of necks and fragments is governed by the competition between the activation of some potential necking and failure points (defects) and the inhibition of some others. Namely, the propagation of release waves from defect points which are activated first leads to the development of obscured zones in which localization and failure is impeded. It is assumed that multiple necking and fragmentation proceed through the random spatial and temporal occurrence of localizations and fractures which result in a distribution of neck spacings and fragment lengths.

An alternative to the statistical theory stemmed from the seminal works of Fressengeas and Molinari (1985, 1994) who approached the problems of multiple necking and fragmentation using dynamic stability analyses. The technique consists of adding a small perturbation to the fundamental solution of the problem to determine whether a neck-like deformation field can exist (Guduru and Freund, 2002). It has been shown that the perturbation grows for a finite number of modes which define the range of neck spacings that can be found in the localization pattern. The existence of growing modes is the result of the combined effects of inertia, stress multiaxiality and constitutive behaviour of the material. The mode that grows the fastest, at each time, is referred to as the critical mode. Rodríguez-Martínez et al. (2013b) demonstrated that, for perfectly plastic materials, the critical mode is associated to the minimum energy required to nucleate a neck. At high strain rates, when inertia plays a dominant role in the loading process, the modes close to the critical one show a clear prevalence over other growing modes, which calls for the development of regular fragmentation patterns (Rodríguez-Martínez et al., 2013a).

The research presented in this paper seeks to provide, using finite element simulations, new insights on the multiple necking process at high strain rates. For that purpose, we investigate through finite element calculations conducted with ABAQUS/Explicit the problem originally posed by Ravi-Chandar and Triantafyllidis (2015) which consists of an incompressible nonlinear elastic bar subjected to dynamic stretching. A localized defect of the strain rate field is included in the model in order to assess whether the defect influences the necking pattern that emerges in the bar at large strains. On the one hand, we have observed that the defect plays a role in the rate of growth of the localization process which develops during the post-uniform deformation regime of the bar. On the other hand, we have shown that the number of nucleated necks and their spacing remain quite insensitive to the defect amplitude, for the range of amplitudes considered in the present work. The latter observation has been rationalized using dynamic stability approaches, and suggests the existence of dominant modes which control (to some extent) the neck spacing in multiple localization patterns developed at high strain rates.

2. Outline of the problem

We address the problem of a cylindrical bar with initial length L^0 and radius R^0 subjected to dynamic stretching. A schematic representation of the problem is shown in Fig. 1, where (R, Θ, Z) denotes the Lagrangian (cylindrical) coordinate system. The initial and boundary conditions for the longitudinal V_Z and radial V_R velocities are:

$$V_Z\left(R,\Theta,Z,0\right)=\dot{\varepsilon}^0 Z; \qquad V_R\left(R,\Theta,Z,0\right)=-\dot{\varepsilon}^0\frac{R}{2}$$

$$V_Z\left(R,\Theta,\pm\frac{L^0}{2},t\right)=\pm\dot{\varepsilon}^0\frac{L^0}{2}$$

where $\dot{\varepsilon}^0$ is the initial strain rate applied to the bar. Moreover, we assume that the bar is initially stress and strain free.

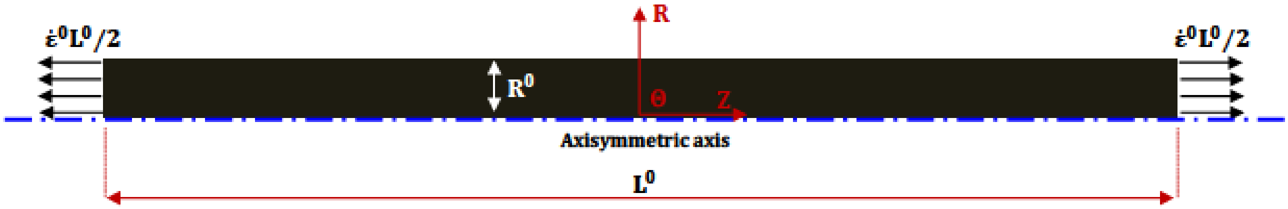

Figure 1: Schematic representation of a cylindrical bar subjected to dynamic stretching.

Following Ravi-Chandar and Triantafyllidis (2015), the material has an incompressible nonlinear elastic behaviour defined by the following power-law relation:

$$\sigma_e = K\varepsilon_e^n \tag{1}$$

where σ_e and ε_e are the effective (Mises) stress and strain, $K = 2$ GPa is a material constant (which defines the stress level for a strain of 1) and $n = 0.22$ is the strain hardening exponent. The material density is $\rho = 7740$ kg/m^3. Following Ravi-Chandar and Triantafyllidis (2015) thermal and viscous effects are not considered in the constitutive behaviour of the material so that the effects of inertia, stress multiaxiality and strain hardening control the instabilities development. Note that during unloading the material follows the nonlinear path defined by Eq. (1).

3. Linear stability models

A two-pronged linear stability approach is used in this work. On the one hand we consider the 3D model developed by Mercier and Molinari (2003) and, on the other, the 1D model enhanced with the Bridgman correction factor developed by Zhou et al. (2006). The goal of this two-pronged strategy is to show that the linear stability approach, irrespective of the degree of complexity of the specific model considered, provides results which are consistent with those obtained from nonlinear numerical calculations (see sections 5 and 6). The initial and loading conditions were presented in section 2.

The linear stability approach, which relies on the seminal works of Fressengeas and Molinari (1985, 1994), is based on the addition of a small perturbation, at a given time, to the fundamental solution of the (homogeneous) problem. Satisfying field equations for the perturbed quantities, the rate of growth of the perturbation η^+ is evaluated. The perturbation growth represents the first stages of the necking pattern. The stabilizing effect of inertia and stress multiaxiality on small and large wavenumbers (respectively) promotes a finite number of intermediate modes. For each strain level, the mode that grows the fastest is characterized by a wavenumber that is referred to as the critical wavenumber ξ_c. The critical wavenumber evolves with strain during the post-uniform regime. As further shown in sections 5 and 6, finite element simulations can be used to determine the duration of the post-uniform regime and identify the strain level for which the rapid localization process is triggered. Performing the linear stability analysis at the localization strain obtained from the finite element calculations it can be shown that the critical wavenumber provides a good estimate of the average localization spacing at high strain rates (Mercier et al., 2010; Rodríguez-Martínez et al., 2013a; Zaera et al., 2015). It will also be shown that accounting for the history of the perturbation growth during the post-uniform deformation process the neck spacing predictions obtained from the linear stability analyses find good agreement with the finite element calculations. For the 1D model, a closed-form expression for η^+ as a function of ξ_c can be derived. For the 3D model, η^+ is the solution of a nonlinear equation that needs to be addressed numerically since no analytical expression can be obtained.

The formulations of the 3D and 1D linear stability models are not presented here for the sake of brevity. The reader is referred to previous publications to obtain further insights into the mathematical derivation of the models (Mercier and Molinari, 2003; Zhou et al., 2006; Rodríguez-Martínez et al., 2013a; El Maï et al., 2014).

4. Finite element model

An axisymmetric finite element model has been developed in ABAQUS/Explicit to simulate multiple necking in cylindrical bars subjected to dynamic stretching. The nonlinear elastic material defined by Eq. (1) is adopted. While the use of strict isochoric materials is not allowed by the numerical code, we have taken a value of the Poisson's ratio which induces for the material, a quite incompressible behavior $\nu = 0.4995$. The initial and loading conditions were presented in section 2. Following the work of Ravi-Chandar and Triantafyllidis (2015), a spatial-localized defect in the axial velocity field is added to the background solution at a given time t^*. Unless otherwise noted the defect is inserted in the center of the bar $Z = 0$ (see Fig. 1):

$$\delta V_Z\left(Z\right) = \alpha\left[\tanh\left(\beta Z + \zeta\right) - \tanh\left(\beta Z - \zeta\right)\right] \tag{2}$$

where α, β and ζ are parameters which control the amplitude, shape and width of the defect. From Eq. (2), the corresponding defect of the strain rate field is obtained:

$$\delta\dot{\varepsilon}_{ZZ}\left(Z\right) = \frac{\partial\left(\delta v_Z\left(Z\right)\right)}{\partial Z} = \alpha\beta\left[\operatorname{sech}\left(\beta Z + \zeta\right)^2 - \operatorname{sech}\left(\beta Z - \zeta\right)^2\right] \tag{3}$$

The velocity and strain rate defects are depicted in Fig. 2 as a function of the axial coordinate Z.

The positions of the extremum of $\delta\dot{\varepsilon}_{ZZ}$, with respect to the center of the defect, are located at Z^{max}:

$$Z^{max} = \pm\operatorname{arcsech}\left(\frac{2}{\sqrt{2 + \cosh(2\zeta) + \sqrt{\frac{17 + 4\cosh(4\zeta)}{2}}}}\right)\beta^{-1} \tag{4}$$

The corresponding amplitude of the strain rate defect $\delta\dot{\varepsilon}_{ZZ}\left(Z^{max}\right)$ can be evaluated analytically as a function of the parameters α, β and ζ, see Fig. 2. While the value of the parameter α is systematically varied in the calculations reported in section 6, the two other parameters are kept

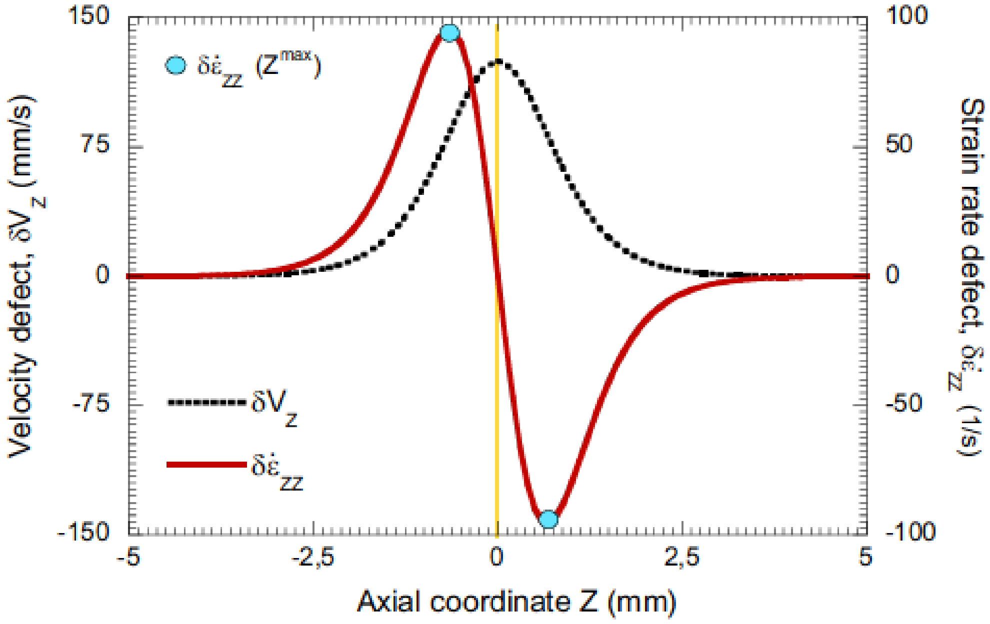

Figure 2: Velocity and strain rate defects, δV_Z and $\delta\dot{\varepsilon}_{ZZ}$, as a function of the axial coordinate Z. The parameters $\alpha = 0.625\ m/s$, $\beta = 1000\ m^{-1}$ and $\zeta = 0.1$ are used.

constant for all the simulations presented in this work: $\beta = 1000\ m^{-1}$ and $\zeta = 0.1$. The defect is added at time $t^* = 0.01\ \mu s$, which corresponds, for the range of strain rates considered in this paper, to strains much smaller than the one predicted by the Considère criterion.

In this paper we will systematically work with strain rate defects. The defect is characterized by its normalized amplitude $\varpi(\%) = \frac{\delta\dot{\varepsilon}_{ZZ}(Z^{max})}{\dot{\varepsilon}^0} \times 100$ where $\delta\dot{\varepsilon}_{ZZ}\left(Z^{max}\right)$ is derived from Eqs. (3) and (4) and, as previously mentioned, $\dot{\varepsilon}^0$ is the initial strain rate. The use of the normalized strain rate amplitude ϖ provides a physical perspective of the problem since there is a direct connection between strain rate and inertia, which facilitates the interpretation of the numerical results (see section 6). Once the defect is inserted in the finite element model, it splits into two parts, each travelling in opposite direction from the other, leading to disturbances in the field variables.

The goal is to provide further insights into the recent work of Ravi-Chandar and Triantafyllidis (2015) and elucidate whether this defect controls/determines the localization pattern which emerges in the bar (see section 6). A key point is that the finite element modelling allows to study the post-uniform behaviour of the rod and thus to analyse the full development of the necking instability. As such, our finite element simulations aim to complement the numerical calculations of Ravi-Chandar and Triantafyllidis (2015) which, being based on the method of characteristics, are restricted to strains below the one obtained from the Considère criterion.

The finite element model is meshed using four node axisymmetric elements, with reduced integration and hourglass control ($CAX4R$). The elements have an initial aspect ratio $1:1$ with dimensions $50 \times 50\ \mu m^2$. A mesh convergence study has been performed, in which the time evolution of different critical output variables, namely stress, strain and necking inception, were compared against different mesh sizes. While we have found some mesh sensitivity in the numerical results, we have checked that it does not affect significantly our results, neither quantitatively nor qualitatively. The number of necks, their spacing and their growth rate are largely independent of the discretization for the cases considered in this paper.

5. Salient features

In this section we present a comparison between numerical and analytical results, and show that flow localization in nonlinear elastic bars stretched at high strain rates is largely influenced by inertia effects.

Fig. 3 shows numerical results for a bar with initial length $L^0 = 40\ mm$ and radius $R^0 = 1\ mm$ subjected to initial strain rate $\dot{\varepsilon}^0 = 10000\ s^{-1}$. This set of values for L^0, R^0 and $\dot{\varepsilon}^0$ is taken as reference in this paper. No strain rate defect is added in the calculations. The necking pattern is triggered by the disturbances of the field variables caused by the discretization of the bar and the explicit integration scheme used by the finite element code (Rusinek and Zaera, 2007; Vadillo et al., 2012; Rodríguez-Martínez et al., 2017). The ratio between the current and the background axial logarithmic strain $\varepsilon_{ZZ}/\varepsilon^b_{ZZ}$ versus the normalized coordinate $\mathcal{Z} = \frac{Z}{L^0}$ is shown for four different times: $t = 46\ \mu s$ and $t = 52\ \mu s$ in Fig. 3(a), $t = 72\ \mu s$ and $t = 74\ \mu s$ in Fig. 3(b). Note that the background strain $\varepsilon^b_{ZZ} = \ln(1+\dot{\varepsilon}^0 t)$ corresponds to the homogeneous solution, where t is the loading time. These four specific loading times are taken to illustrate the inception and development of multiple necks in the specimen.

For $t = 46\ \mu s$ the background strain, which has a value of 0.38, is significantly greater than the Considère strain 0.22 (see Eq. (1)). We observe some slight fluctuations in the strain profile which indicate the onset of the localization pattern. The excursions of strain represent the nucleation of necks. All the bar is perturbed following a neck-like profile. The maximum value of the ratio $\varepsilon_{ZZ}/\varepsilon^b_{ZZ}$ is ≈ 1.0003. For $t = 52\ \mu s$ the background strain is 0.419. The localization pattern has evolved and the maximum value of the ratio $\varepsilon_{ZZ}/\varepsilon^{b}_{ZZ}$ is ≈ 1.0007. Moreover, in comparison with the strain field observed for $t = 46$ μs, two additional excursions are observed (see the indications in Fig. 3(a)). There is a total of 13 necking points. It is apparent that the necking pattern is progressively built up during the post-uniform deformation regime. This is because inertia has a stabilizing effect and delays the formation and development of necks (Xue et al., 2008). It is also observed that the necks located in the centre of the specimen develop slightly faster than those which are closer to the sample ends. This suggests an influence of the boundary conditions in the localization process (we will further develop this issue in section 6.3). For $t = 72$ μs the background strain is 0.542. The necking pattern is very much developed and the strain excursions are well defined. The maximum value of the ratio $\varepsilon_{ZZ}/\varepsilon^{b}_{ZZ}$ is ≈ 1.2. The number of strain excursions and their location coincide with those observed for $t = 52$ μs. The necking pattern does not undergo any additional modification with the straining of the bar. The average normalized Lagrangian neck spacing is $\bar{L}^{neck}/\Phi^{0} = 1.54$, where $\bar{L}^{neck}$ is the mean distance between two consecutive necks measured in the reference configuration and $\Phi^{0} = 2R^{0}$ is the initial diameter. We observe in the histogram presented in Fig. 4 that the normalized distances between two consecutive necks L^{neck}/Φ^{0} present some fluctuations but are centred around (and close to) the average normalized spacing $\bar{L}^{neck}/\Phi^{0}$. Moreover, the Weibull probability density function given in Eq. (5) has been fitted to the numerical results (blue solid line). The parameters of the distribution are $\chi = 2.98$, $\kappa = 7.12$ and $\lambda = 1.51$.

$$fw\left(\frac{L^{neck}}{\Phi^{0}}\right) = \chi\frac{\kappa}{\lambda}\left(\frac{L^{neck}}{\lambda\Phi^{0}}\right)^{\kappa-1} e^{\left(\frac{-L^{neck}}{\lambda\Phi^{0}}\right)^{\kappa}} \tag{5}$$

While the number of necks in the bar is not large, it has to be noted that, consistently with the results of Zhang and Ravi-Chandar (2006), the Weibull distribution fits the measured neck spacings rather well. For $t = 74$ μs the necking pattern is fully developed. The ratio between the maximum and the background axial logarithmic strain is ≈ 1.6. Inside the necked sections the strain grows quickly and outside the localized regions the strain drops due to elastic unloading. Note that none of the necks is arrested. In absence of any dissipative source, all the energy released in the unloaded zones serves to boost the growth of the necks.

Note that, during loading, nonlinear elastic and elasto-plastic materials defined by Eq. (1) show identical response. However, if unloading occurs, their behavior is significantly different.

In other words, the results reported in this paper are specific for nonlinear elastic bars and, in principle, could not be extrapolated to elasto-plastic specimens. The interaction between the necks of the pattern could be affected by the unloading process. Moreover, for elasto-plastic materials, the dissipative character of plasticity will probably influence the growth rate of the necks. In addition, a different fragmentation behavior is expected between nonlinear elastic and elasto-plastic materials. The comparison between the necking and fragmentation responses of nonlinear elastic and elasto-plastic structures is an ongoing work.

Fig. 5 shows the axial force F_Z measured at one end of the specimen versus the loading time t and the axial nominal strain $e_{ZZ} = \dot{\varepsilon}^0 t$ for the calculation presented in Fig. 3. We have checked that the forces recorded at both ends of the sample are nearly identical. Note that the post-uniform deformation regime is very large and lasts longer than the uniform deformation process. This is a clear manifestation of the stabilizing effect of inertia in the loading process, as further demonstrated in section 6.1. Recall that the material behaviour is rate insensitive. For the case considered here, the uniform deformation process ends at the Considère strain 0.22, while the post-uniform deformation regime has an extent in strain of ≈ 0.5. The force shows a meaningful deviation from the fundamental solution, represented by the green solid line, only for $t \gtrsim 70 \mu s$. The numbers 1, 2, 3 and 4 indicate the four loading times considered in Fig. 3. It is apparent that, at high strain rates, the core of the localization process occurs at strains much larger that the Considère strain. In other words, the existence of a meaningful post-uniform deformation process cannot be disregarded in the analysis of multiple necking at high strain rates.

The numerical results presented above are further rationalized using the linear stability analyses. Fig. 6 shows analytical results obtained from the 1D and 3D linear stability models introduced in section 4. As in the numerical results presented in Figs. 3, 4 and 5, the cross-section radius of the bar is $R^0 = 1\ mm$ and the nominal loading rate is $\dot{\varepsilon}^0 = 10000\ s^{-1}$. We plot the average normalized Lagrangian neck spacing $\bar{L}^{neck}/\Phi^0$ versus the axial logarithmic strain ε_{ZZ}. The average Lagrangian neck spacing is derived from the critical wavenumber ξ_c as $\bar{L}^{neck} = 2\pi/\xi_c$ (see section 3). We observe that 3D and 1D models provide similar values, which shows the suitability of the Bridgman correction used in the 1D model to describe the multiaxial stress state in the necked section. The only difference is that the 3D model provides slightly larger values of $\bar{L}^{neck}/\Phi^0$ in the range of strains considered. Irrespective of the selected analytical model, the average normalized

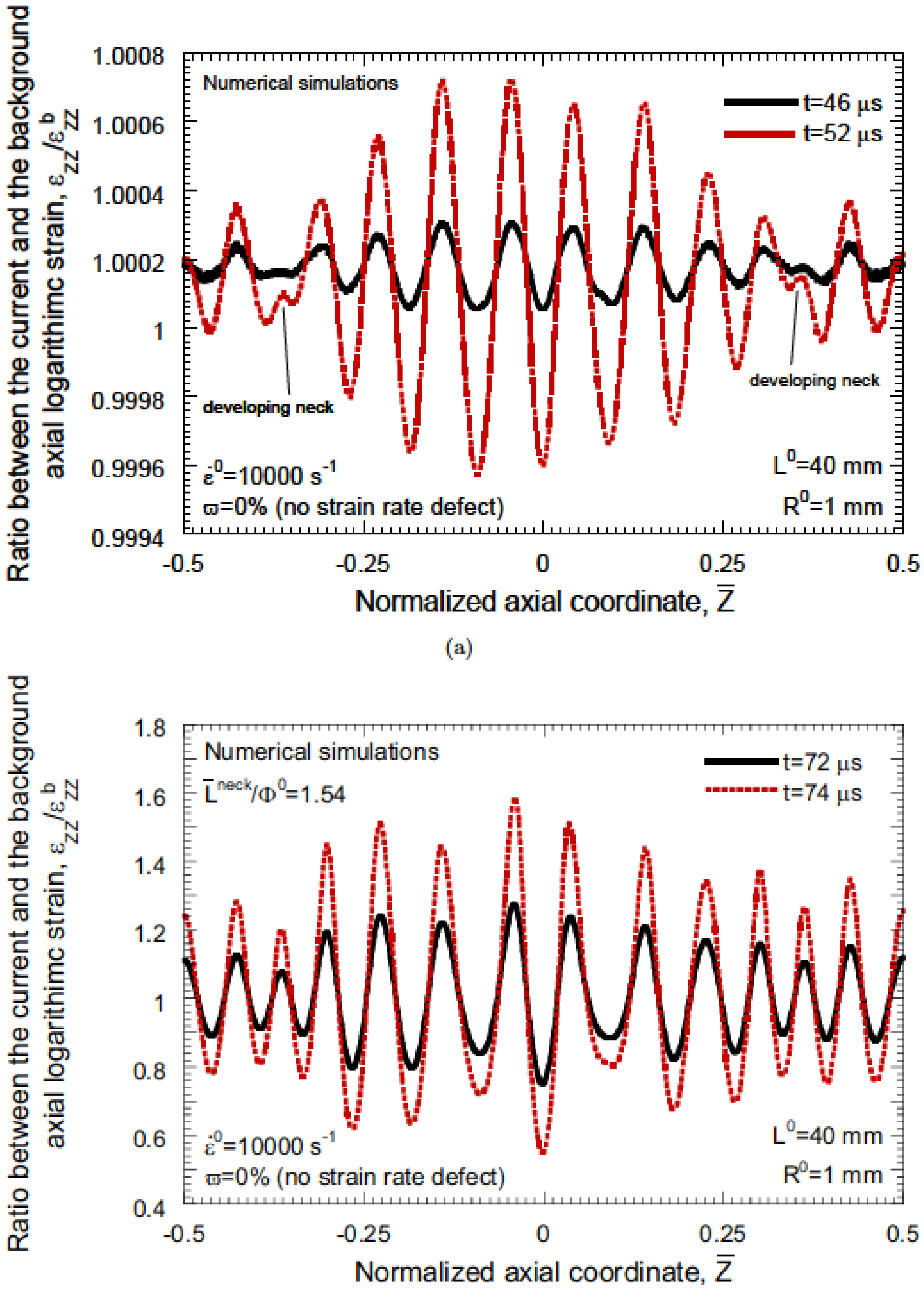

(a)

(b)

Figure 3: Ratio between the current and the background axial logarithmic strain $\varepsilon_{ZZ}/\varepsilon_{ZZ}^b$ versus the normalized coordinate $\bar{Z} = \frac{Z}{L^0}$ at four different loading times: (a) $t = 46\ \mu s$ and $t = 52\ \mu s$ (b) $t = 72\ \mu s$ and $t = 74\ \mu s$. A finite element calculation is presented for $L^0 = 40\ mm$ and $R^0 = 1\ mm$. The initial strain rate is $\dot{\varepsilon}^0 = 10000\ s^{-1}$. No strain rate defect is included in the model.

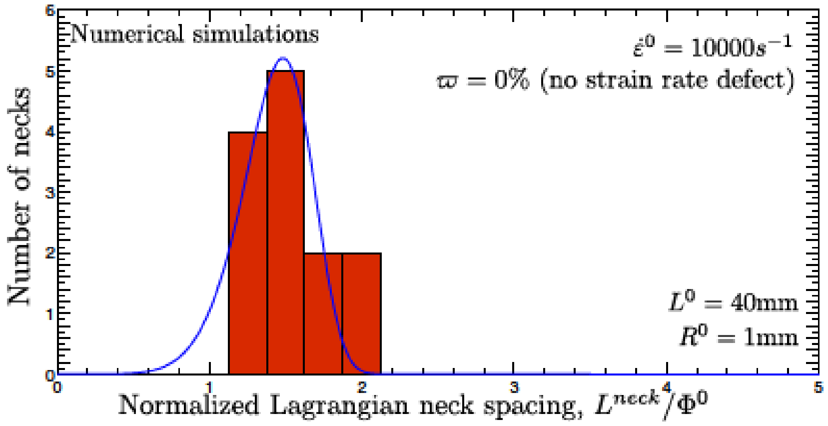

Figure 4: Histogram which presents the number of necks as a function of the normalized Lagrangian neck spacing L^{neck}/Φ^0. The results correspond to the finite element calculation presented in Fig. 3. A Weibull probability density function (blue solid line) has been fitted to the numerical results. The parameters of the Weibull distribution are $\chi = 2.98$, $\kappa = 7.12$ and $\lambda = 1.51$.

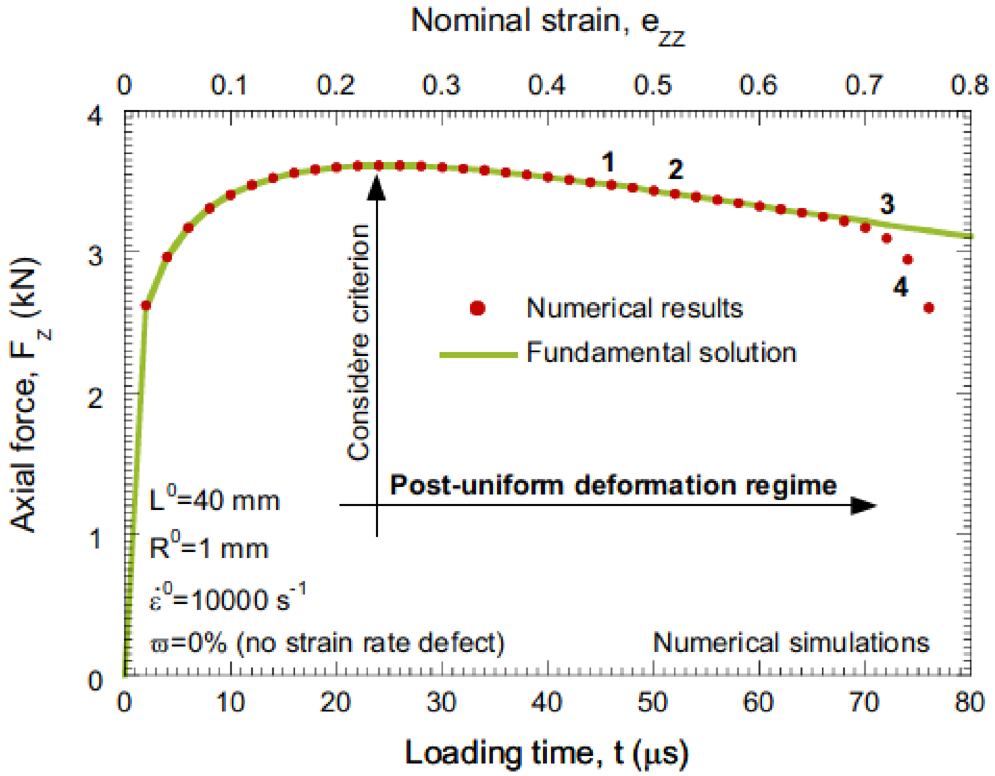

Figure 5: Axial force F_Z versus loading time t and axial nominal strain $e_{ZZ} = \dot{\varepsilon}^0 t$. The results correspond to the finite element calculation presented in Fig. 3. The numbers 1, 2, 3 and 4 indicate the four loading times considered in Fig. 3. The solid green line represents the fundamental solution.

Lagrangian neck spacing decreases with ε_{ZZ}, i.e. the average neck spacing is smaller as ε_{ZZ} increases. The decrease of $\bar{L}^{neck}/\Phi^0$ is significantly milder as the strain at perturbation increases.

Note that linear stability analyses are only valid to describe the first stages of the necking pattern development (see section 3), in other words, when the neck-like deformation field shows only a small deviation from the background strain (see Fig. 3). In that case the force exerted in the bar is close to the fundamental solution (see Fig. 5). Based on the finite element analysis, the loading time which defines the upper limit for the application of the linear stability analysis in the specific case of Fig. 6 is $t \approx 70\ \mu s$. This loading time, which corresponds to a drastic drop in the force, yields a background logarithmic strain of $\varepsilon_{ZZ} \approx 0.53$ (note that Fig. 5 shows nominal strains e_{ZZ} and that $\varepsilon_{ZZ} = \ln(1 + e_{ZZ})$). On the other hand, the definition of the lower limit for the application of the linear stability analysis shows more arbitrariness. In this work, we assume that the minimum deviation from the fundamental solution required to obtain meaningful pattern predictions using the stability analysis occurs when the deformation field of the bar reaches (in some point of the bar) a ratio between the current and the background axial logarithmic strain of 1.0003. It has been observed in the numerical simulations that this is the minimum ratio required for the formation of a well defined neck-like profile. In the specific case of Fig. 6, previous condition is attained for a loading time of $t \approx 46\ \mu s$ and thus a background logarithmic strain of $\varepsilon_{ZZ} \approx 0.38$. Following previous criteria, the predictions of the stability models in Fig. 6 are evaluated within the range of axial logarithmic strains $0.38 \lesssim \varepsilon_{ZZ} \lesssim 0.53$. For the 1D and 3D models these values of strain correspond to average neck spacings within the ranges $1 \lesssim \bar{L}^{neck}/\Phi^0 \lesssim 1.37$ and $1 \lesssim \bar{L}^{neck}/\Phi^0 \lesssim 1.48$, respectively. These results, especially in the case of the 3D model, find satisfactory correlation with finite element calculations for which $\bar{L}^{neck}/\Phi^0 = 1.54$.

In the next section of the paper we develop a systematic comparison of numerical simulations in which a spatial-localized defect of different amplitudes is included. A wide spectrum of loading rates and sample sizes is investigated.

6. Analysis and results

The analysis carried out in this section is mostly based on numerical calculations. Additionally, the linear stability analyses are used to rationalize our conclusions.

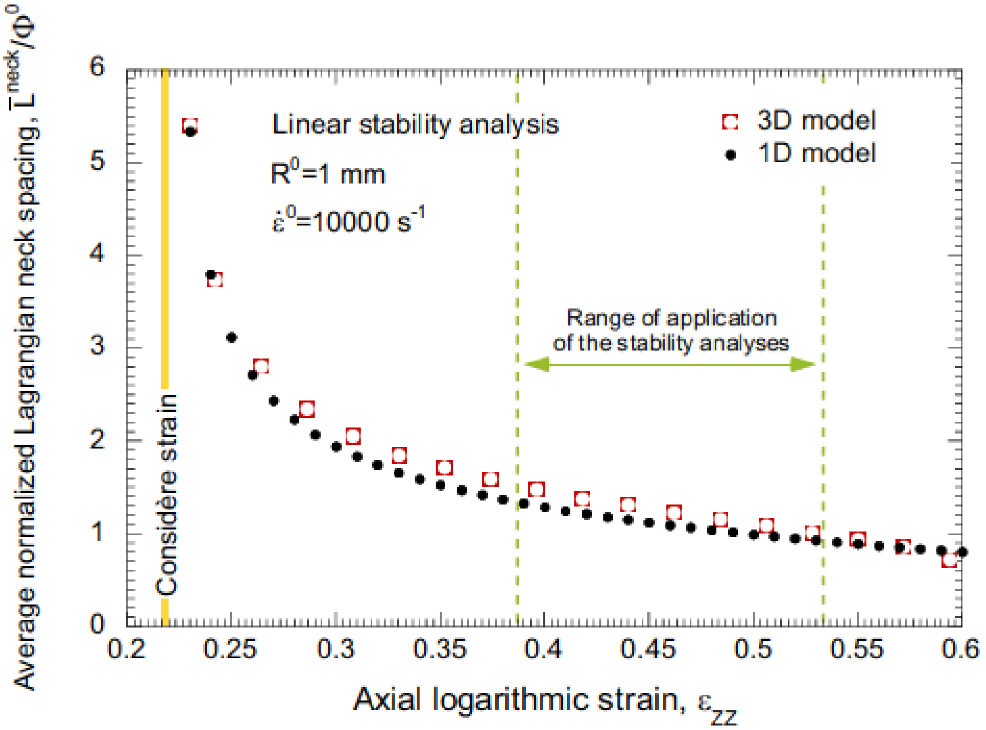

Figure 6: Average normalized Lagrangian neck spacing $\bar{L}^{neck}/\Phi^0$ versus axial logarithmic strain ε_{ZZ}. Results are shown for 1D and 3D linear stability models. The configuration of Fig. 3 is adopted.

6.1. The role of the loading rate

We investigate the role played by the loading rate on flow localization. Fig. 7 shows the average normalized Lagrangian neck spacing $\bar{L}^{neck}/\Phi^0$ versus the initial loading rate $\dot{\varepsilon}^0$. These results are obtained from numerical calculations in which a strain rate defect is inserted in the center of the specimen. Various normalized defect amplitudes within the range $0.12\% \leq \varpi \leq 7.65\%$ are investigated. Note that the latter is a very significant defect of the strain rate field. A special attention is also drawn for the case without any defect $\varpi = 0\%$ (as in section 5). For some loading rates, due to similar results, some symbols overlap each other and are not visible. Note that, irrespective of ϖ, the average neck spacing decreases with the strain rate. As demonstrated by Rodríguez-Martínez et al. (2013a), this behaviour is mostly caused by the increasing role played by inertia on flow localization as the loading rate increases. Similar results have been obtained experimentally, numerically and analytically by several authors for various ductile materials (Grady and Benson, 1983; Hu and Daehn, 1996; Grady and Olsen, 2003; Mercier and Molinari, 2004; Zhang and Ravi-Chandar, 2006; Rusinek and Zaera, 2007).

Fig. 8 shows the ratio between the current and the background axial logarithmic strain $\varepsilon_{ZZ}/\varepsilon^b_{ZZ}$

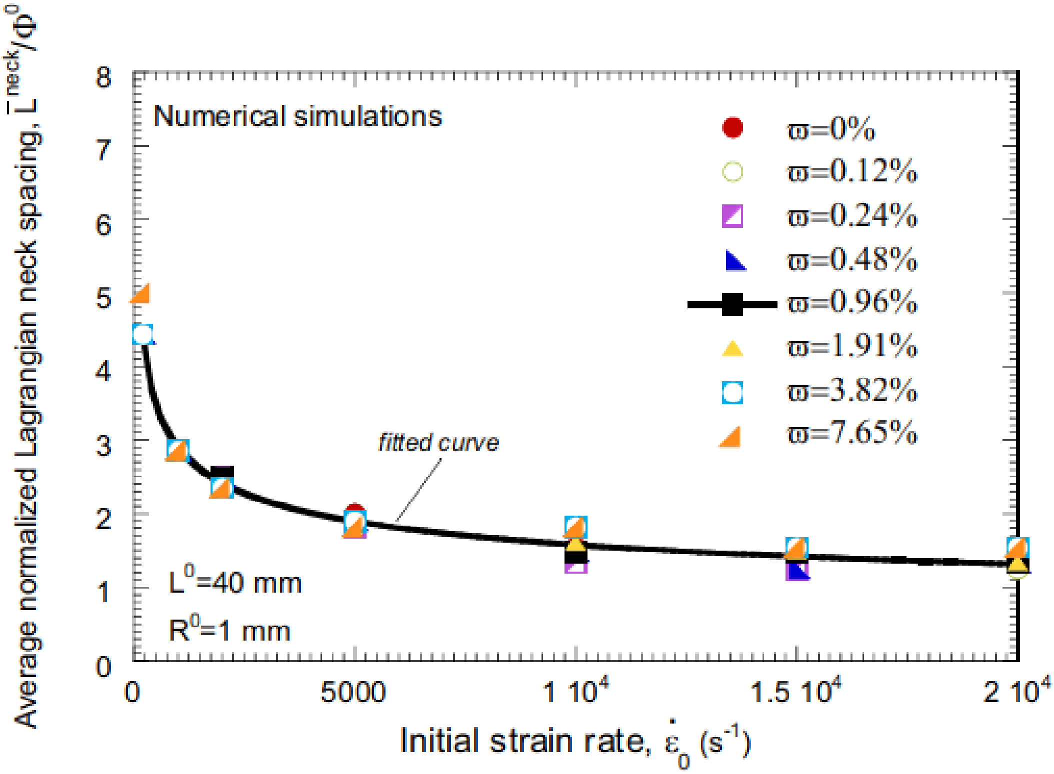

Figure 7: Average normalized Lagrangian neck spacing $\bar{L}^{neck}/\Phi^0$ versus initial loading rate $\dot{\varepsilon}^0$. Results are obtained using finite element calculations for seven normalized defect amplitudes: $\varpi = 0.12\%$, $\varpi = 0.24\%$, $\varpi = 0.48\%$, $\varpi = 0.96\%$, $\varpi = 1.91\%$, $\varpi = 3.82\%$ and $\varpi = 7.65\%$. The defect is included at the center of the specimen. Results in which no defect is included in the model ($\varpi = 0\%$) are shown also. The initial length and radius of the bar are $L^0 = 40\ mm$ and $R^0 = 1\ mm$. Note that, for some loading rates, due to similar results, some symbols overlap each other and are not visible.

as a function of the normalized coordinate $\bar{Z}$ for three different loading rates: $\dot{\varepsilon}^0 = 200\ s^{-1}$, $\dot{\varepsilon}^0 = 2000\ s^{-1}$ and $\dot{\varepsilon}^0 = 20000\ s^{-1}$. The amplitude of the strain rate defect is $\varpi = 0.96\%$. Recall that the defect is inserted in the simulation at $t^* = 0.01\ \mu s$. The data shown in Fig. 8 for the three loading rates correspond to $t = 1456\ \mu s$, $t = 208\ \mu s$ and $t = 50\ \mu s$, respectively. These specific loading times are selected in order to obtain the same maximum value of the ratio $\varepsilon_{ZZ}/\varepsilon^b_{ZZ}$ (around 1.6). Thus, we ensure that the localization pattern is fully developed. On the one hand, we have checked that the values of strain corresponding to the peaks of Fig. 8 are more homogeneous as the strain rate increases. On the other hand, none of the examples presented in Fig. 8 shows any evidence of the (potential) effect of the strain rate defect in the localization pattern.

In this regard, we should note that the normalized amplitude of the strain $\varepsilon_{ZZ}/\varepsilon^b_{ZZ}$ (current strain divided by background axial logarithmic strain) decreases in the pre-Considère regime and increases once the Considère strain is exceeded. Fig. 9 presents the normalized strain profiles within the bar for six different loading times $t = 1$ to $t = 35$ microseconds. Note that the three first times correspond to background strains in the pre-Considère regime, Fig. 9(a), while for the last three times, the background strains are in the post-Considère phase, Fig. 9(b). In Fig. 9(a), it is clear that the defect propagates along the bar. The relative strain amplitude is decreasing. When the Considère strain is reached the defects are arrested at given positions of the bar. For strains above the Considère strain the amplitude of the defect increases with the stretching of the structure. In addition to the strain rate defect, other instability modes are gradually activated within the bar. All these modes develop until the necking pattern shown in Fig. 8 is formed.

Moreover, we have compared the results of Fig. 8 with calculations in which ϖ was set to zero. The comparison for the case of $\dot{\varepsilon}^0 = 2000\ s^{-1}$ is shown in Fig. 10. It seems that for $\varpi = 0.96\%$ and $\dot{\varepsilon}^0 = 2000\ s^{-1}$ the defect plays a secondary role in the necking pattern. The influence of the defect amplitude in the necking pattern will be further discussed in section 6.2.

Fig. 11 displays the axial force F_Z measured at one end of the sample versus the axial nominal strain $e_{ZZ} = \dot{\varepsilon}^0 t$ for the numerical simulations of Fig. 8. We observe that the post-uniform deformation regime is significantly enlarged with the strain rate. Numbers 1, 2 and 3 indicate the specific loading times selected in Fig. 8 for $\dot{\varepsilon}^0 = 200\ s^{-1}$, $\dot{\varepsilon}^0 = 2000\ s^{-1}$ and $\dot{\varepsilon}^0 = 20000\ s^{-1}$, respectively. These loading times coincide with the beginning of the localization stage where the force in the bar deviates from the fundamental solution. For $\dot{\varepsilon}^0 = 200\ s^{-1}$ the post-uniform regime

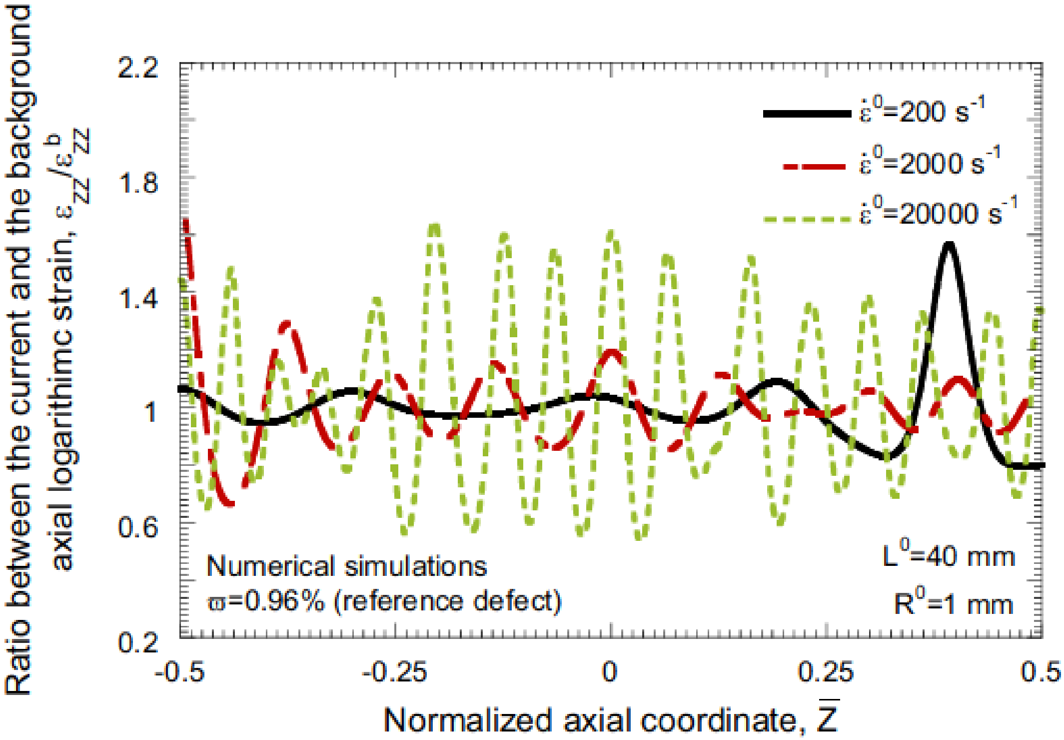

Figure 8: Ratio between the current and the background axial logarithmic strain $\varepsilon_{ZZ}/\varepsilon^b_{ZZ}$ versus the normalized coordinate $\bar{Z} = \frac{Z}{L^0}$. Results are obtained using finite element calculations with three different initial loading rates: $\dot{\varepsilon}^0 = 200\ s^{-1}$, $\dot{\varepsilon}^0 = 2000\ s^{-1}$ and $\dot{\varepsilon}^0 = 20000\ s^{-1}$. A strain rate defect with normalized amplitude $\varpi = 0.96\%$ has been introduced in the center of the specimen. The data shown for the three initial loading rates correspond to $t = 1456\ \mu s$, $t = 208\ \mu s$ and $t = 50\ \mu s$, respectively. These times are selected in order to nearly obtain the same maximum value of the ratio $\varepsilon_{ZZ}/\varepsilon^b_{ZZ}$ (around 1.6) for the three calculations. The initial length and radius of the bar are $L^0 = 40\ mm$ and $R^0 = 1\ mm$.

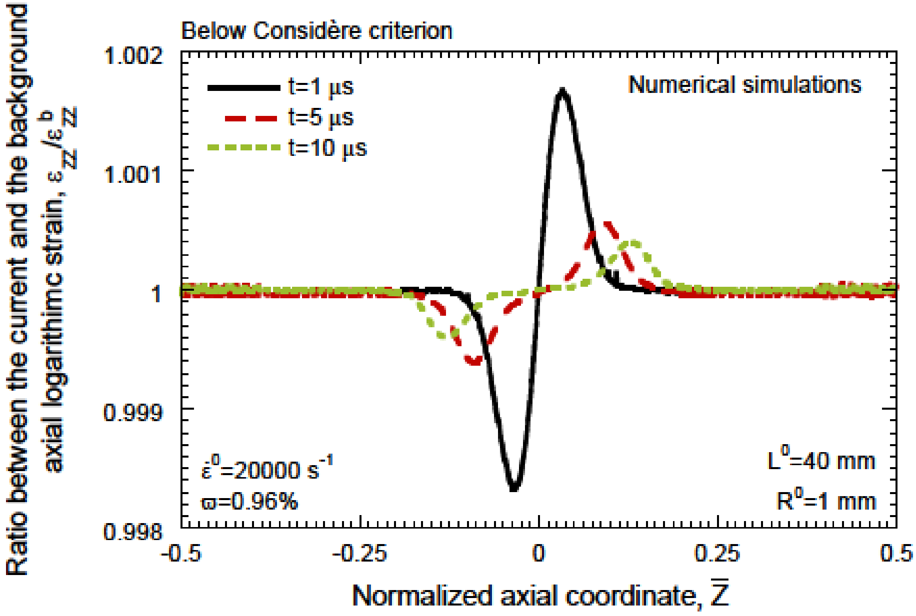

(a)

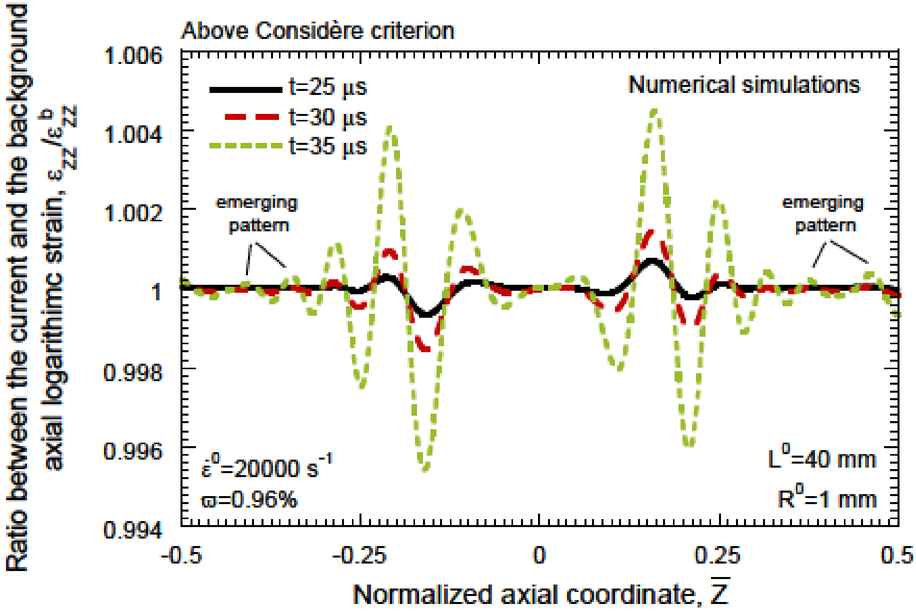

(b)

Figure 9: Ratio between the current and the background axial logarithmic strain $\varepsilon_{ZZ}/\varepsilon^b_{ZZ}$ versus the normalized coordinate $\bar{Z} = \frac{Z}{L^0}$. Results are obtained using a finite element calculation for $\dot{\varepsilon}^0 = 20000\ s^{-1}$. A strain rate defect with normalized amplitude $\varpi = 0.96\%$ has been introduced in the center of the specimen. Data are shown for six different loading times: (a) $t = 1\ \mu s$, $t = 5\ \mu s$ and $t = 10\ \mu s$ which correspond to backgrounds strains below the Considère criterion: $\varepsilon^b_{ZZ} = 0.020$, $\varepsilon^b_{ZZ} = 0.095$ and $\varepsilon^b_{ZZ} = 0.182$. (b) $t = 25\ \mu s$, $t = 30\ \mu s$ and $t = 35\ \mu s$ which correspond to backgrounds strains above the Considère criterion: $\varepsilon^b_{ZZ} = 0.405$, $\varepsilon^b_{ZZ} = 0.470$ and $\varepsilon^b_{ZZ} = 0.530$. The initial length and radius of the bar are $L^0 = 40\ mm$ and $R^0 = 1\ mm$.

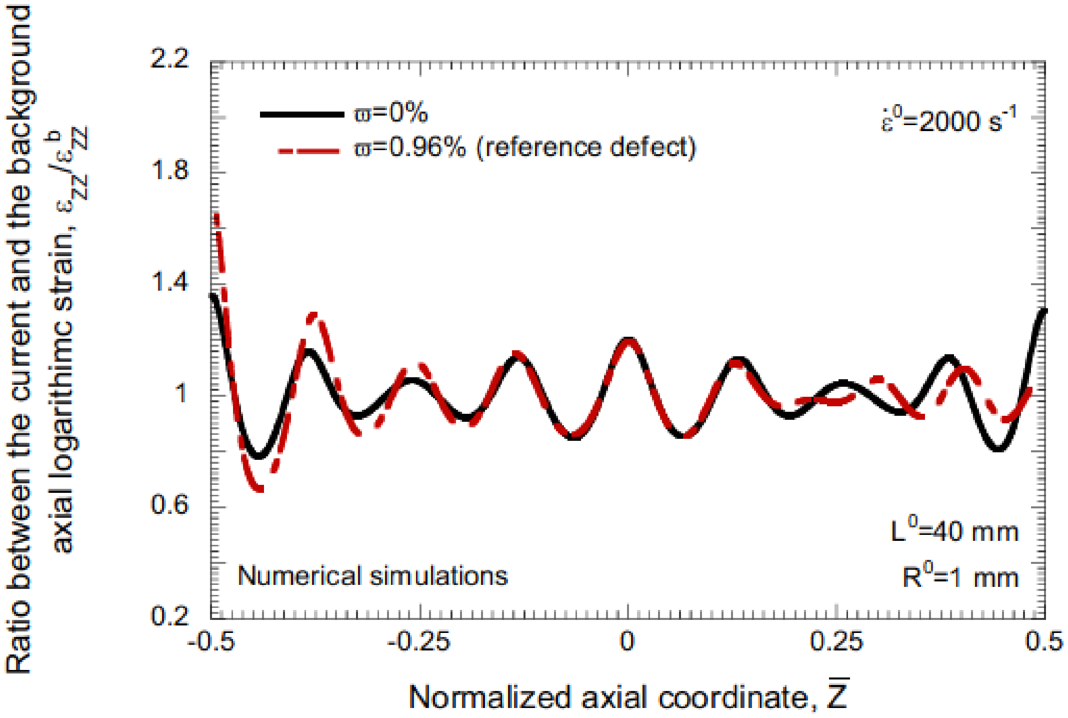

Figure 10: Ratio between the current and the background axial logarithmic strain $\varepsilon_{ZZ}/\varepsilon^{b}_{ZZ}$ versus the normalized coordinate $\bar{Z} = \frac{Z}{L^0}$. Results are obtained using finite element calculations with two different normalized strain rate defect amplitudes: $\varpi = 0\%$ (no defect) and $\varpi = 0.96\%$ (reference defect). The defect is included at the center of the specimen. The initial strain rate is $\dot{\varepsilon}^0 = 2000\ s^{-1}$. The data shown correspond to $t = 208\ \mu s$. The initial length and radius of the bar are $L^0 = 40\ mm$ and $R^0 = 1\ mm$.

has a limited strain extension. The necking pattern is incepted and developed shortly after the force reached a maximum. On the contrary, for $\dot{\varepsilon}^0 = 20000\ s^{-1}$ the localization is delayed until very large strains are attained in the bar. We also observe that the drop of the force corresponding to the late stages of the localization process is significantly slowed down as $\dot{\varepsilon}^0$ increases. As anticipated in section 5, the stabilizing role of inertia at high strain rates favours the development of a large post-uniform deformation regime which needs to be considered in the analysis of multiple necking problems. Since no failure criterion is used in the calculations, the strain in the sample increases freely until the excessive distortion of the elements in the necked sections stops the simulation.

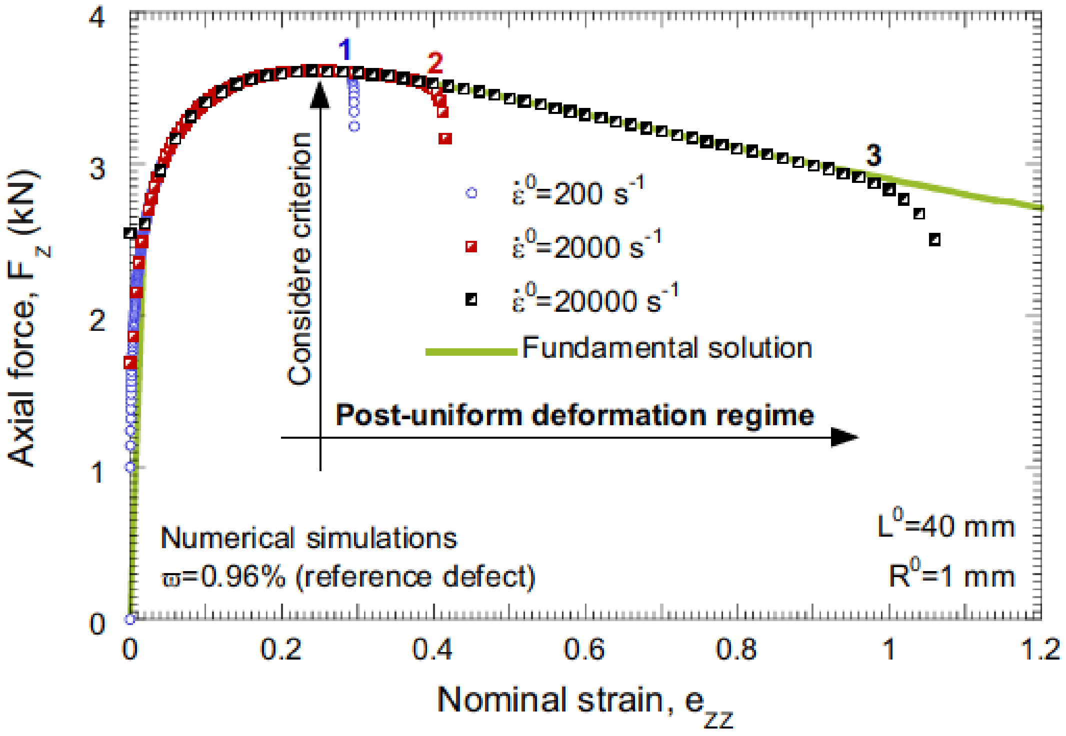

Figure 11: Axial force F_Z versus axial nominal strain $e_{ZZ} = \dot{\varepsilon}^0 t$ for the three finite element calculations presented in Fig. 8. The numbers 1, 2 and 3 point out the loading times selected in Fig. 8 for $\dot{\varepsilon}^0 = 200\ s^{-1}$, $\dot{\varepsilon}^0 = 2000\ s^{-1}$ and $\dot{\varepsilon}^0 = 20000\ s^{-1}$, respectively. The solid green line represents the fundamental solution.

Fig. 12 shows the average normalized Lagrangian spacing L^{neck}/Φ^0 versus the normalized initial location of the defect $\bar{Z} = \frac{Z}{L^0}$. Nine different initial locations of the defects are explored: $\bar{Z} = \pm 0.5$, $\bar{Z} = \pm 0.375$, $\bar{Z} = \pm 0.25$, $\bar{Z} = \pm 0.125$ and $\bar{Z} = 0$. The amplitude of the strain rate defect included in the numerical calculations is $\varpi = 0.96\%$. Note that this is the only graph in the paper with results obtained from numerical simulations in which the defect was not located in the center of the specimen. As in previous plots, the initial length and radius of the bar are $L^0 = 40\ mm$ and $R^0 = 1\ mm$, respectively. The initial strain rate is $\dot{\varepsilon}^0 = 10000\ s^{-1}$. We observe that the average necks spacing is largely independent of the position of the bar where the defect is included: this further shows that the defect seems to play a secondary role in the necks spacing.

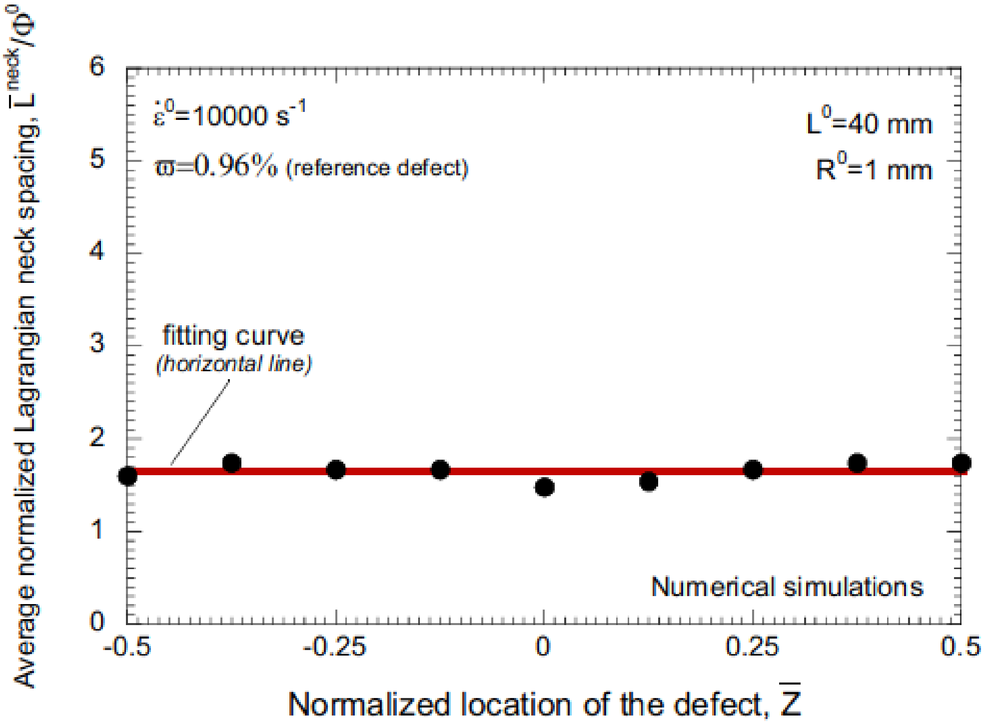

Figure 12: Average normalized Lagrangian neck spacing $\bar{L}^{neck}/\Phi^0$ versus normalized location of the defect $\bar{Z} = \frac{Z}{L^0}$. Results are obtained using finite element calculations in which nine different locations of the defect are explored: $\bar{Z} = \pm 0.5$, $\bar{Z} = \pm 0.375$, $\bar{Z} = \pm 0.25$, $\bar{Z} = \pm 0.125$ and $\bar{Z} = 0$. The amplitude of the strain rate defect included in the numerical calculations is $\varpi = 0.96\%$. The initial length and radius of the bar are $L^0 = 40\ mm$ and $R^0 = 1\ mm$. The initial strain rate is $\dot{\bar{\varepsilon}}^0 = 10000\ s^{-1}$.

In Fig. 13 we compare, for various loading rates, the average normalized Lagrangian neck spacing $\bar{L}^{neck}/\Phi^0$ obtained from the numerical simulations for the case of $\varpi = 0.96\%$ with the predictions of the stability analyses. The perturbation is inserted at the time when the force deviates from the fundamental solution in the corresponding numerical calculation. It is observed that both 1D and 3D stability models predict values of the spacing which are quite similar. In addition, the evolution of the neck spacing with the strain rate predicted by the stability analyses follows the trend obtained from the finite element calculations. As the strain rate increases, the average neck spacing decreases and the strain at localization increases, see Table 1. Nevertheless, there is some discrepancy between analytical and numerical predictions, see Fig. 13.

In this regard, since the critical wavenumber in the stability analyses varies with time (i.e. deformation), it is worth tracking the history of the growth rate of all the growing modes during the deformation process. Thus, as originally proposed by Fressengeas and Molinari (1994) and

Strain rate [s^{-1}]	Strain - FE	time [μs] - FE	Strain - 1D LSA	time [μs] - 1D LSA	Strain - 3D LSA	time [μs] - 3D LSA
200	0.256	1456	0.256	1456	0.256	1456
1000	0.298	348	0.303	357	0.303	357
2000	0.347	208	0.340	202	0.344	205
5000	0.412	102	0.416	103	0.427	106
10000	0.512	67	0.507	66	0.525	69

Table 1: Predictions of the localization strain and time using 1D and 3D linear stability analyses (referred to as LSA) together with the cumulative instability index I. The predictions of the stability analyses are in good agreement with the finite element simulations (referred to as FE). The instability index is set to $I_c = 10.16$ for the 1D model and $I_c = 10.04$ for the 3D model to obtain the analytical predictions. These values have been calibrated using the lowest strain rate case 200 s^{-1}.

later adopted by Petit et al. (2005) and El Maï et al. (2014), an alternative critical wavenumber is identified relying on the evolution of a cumulative instability index defined as $I = \int_{t_{\text{considère}}}^{t} \eta^+ dt$ where $t_{\text{considère}}$ corresponds to the time of maximum force. El Maï et al. (2014) have shown that the neck spacing predicted using the critical wavenumber associated to the cumulative instability index I is greater than the neck spacing derived from the critical wavenumber associated to the instantaneous instability index η^+. Within this context, the following methodology has been adopted to calibrate the critical value of the cumulative instability index I. First, the case of initial strain rate 200 s^{-1} is considered. The finite element simulations predict that the localization occurs at $t = 1456$ μs. The linear stability analyses are performed from $t_{\text{considère}}$ to $t = 1456$ μs and the cumulative index I is calculated. The wavenumber which presents the largest cumulative growth rate (the critical wavenumber) is $\xi_c = 787$ m^{-1} for the 1D model and $\xi_c = 785$ m^{-1} for the 3D model. The corresponding values of the index I are $I_c = 10.16$ and $I_c = 10.04$, respectively. Next, we consider cases with larger nominal strain rate varying from 1000 s^{-1} to 10000 s^{-1}. For each nominal strain rate, the critical wavenumber, the time and the strain at which the condition $I = I_c$ is met, are determined. Fig. 13 shows that the neck spacings predicted with the cumulative instability index, using 1D and 3D models, are in close agreement with the results obtained from the finite element calculations within the whole range of strain rates considered here. Note also that the corresponding strains and times when $I = I_c$ are in good agreement with the values provided by the finite element calculations, see Table 1. The values of I_c are valid for a given material, geometry, amplitude and shape of defect.

In the next section of the paper, we further investigate the interplay between the strain rate defect and the necking pattern.

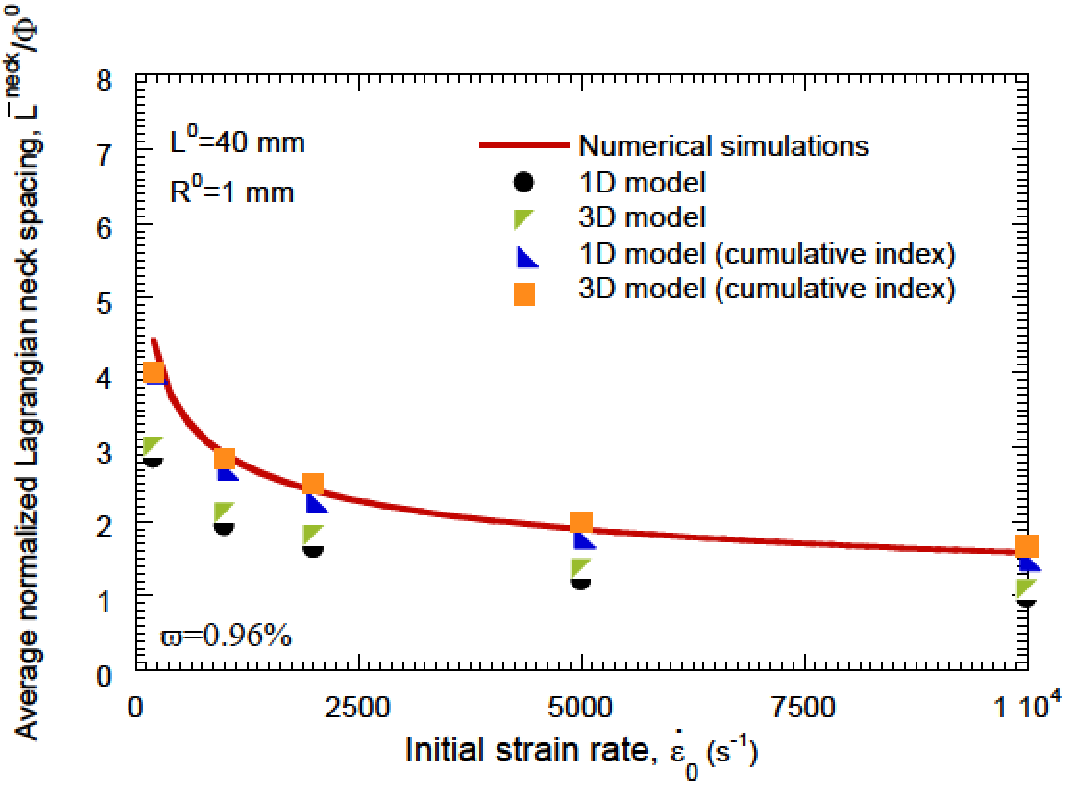

Figure 13: Comparison between finite element calculations and linear stability analyses. Average normalized Lagrangian neck spacing $\bar{L}^{neck}/\Phi^0$ versus initial loading rate $\dot{\varepsilon}^0$. The amplitude of the strain rate defect included in the numerical calculations is $\varpi = 0.96\%$. The initial length and radius of the bar are $L^0 = 40\ mm$ and $R^0 = 1\ mm$.

6.2. The role of defect amplitude

Fig. 14 shows the average normalized Lagrangian neck spacing $\bar{L}^{neck}/\Phi^0$ versus the dimensionless defect amplitude $\varpi(\%)$ for various loading rates ranging between $\dot{\varepsilon}^0 = 200\ s^{-1}$ and $\dot{\varepsilon}^0 = 20000\ s^{-1}$. Note that, irrespective of the value of $\dot{\varepsilon}^0$, the average neck spacing is largely insensitive to the defect amplitude (see also Fig. 7). We observe only for the highest values of ϖ a slight increase of $\bar{L}^{neck}/\Phi^0$. These numerical simulations suggest the existence of a dominant wavelength which characterizes (at least to some extent) the average neck spacing, in agreement with the theoretical predictions based on modal analysis arguments, e.g. Fressengeas and Molinari (1985, 1994); Mercier and Molinari (2003, 2004); Rodríguez-Martínez et al. (2013a, 2015).

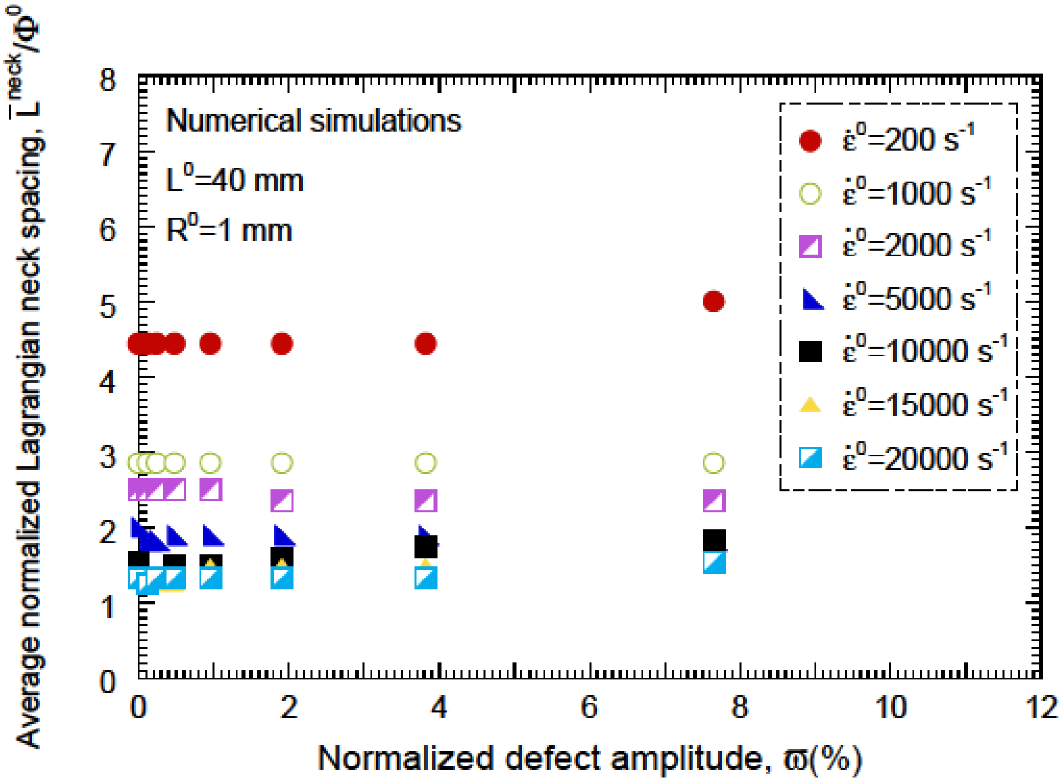

Figure 14: Average normalized Lagrangian neck spacing $\bar{L}^{neck}/\Phi^0$ versus normalized defect amplitude $\varpi(\%)$. Results are obtained using finite element simulations with seven initial loading rates: $\dot{\varepsilon}^0 = 200\ s^{-1}$, $\dot{\varepsilon}^0 = 1000\ s^{-1}$, $\dot{\varepsilon}^0 = 2000\ s^{-1}$, $\dot{\varepsilon}^0 = 5000\ s^{-1}$, $\dot{\varepsilon}^0 = 10000\ s^{-1}$, $\dot{\varepsilon}^0 = 15000\ s^{-1}$ and $\dot{\varepsilon}^0 = 20000\ s^{-1}$. The defect is included at the center of the specimen. The initial length and radius of the bar are $L^0 = 40\ mm$ and $R^0 = 1\ mm$.

Fig. 15 shows the axial force F_Z measured at one end of the specimen versus loading time t and axial nominal strain $e_{ZZ} = \dot{\varepsilon}^0 t$ for simulations with three defect amplitudes: $\varpi = 0.48\%$, $\varpi = 0.96\%$ (reference case) and $\varpi = 3.82\%$. The initial loading rate is $\dot{\varepsilon}^0 = 10000\ s^{-1}$. Despite the strain rate defect included in the simulations, the deformation field of the bar remains close to the fundamental solution beyond the Considère strain. The stabilizing effect of inertia overcomes the destabilizing role of the defect and delays the localization of the deformation. Differences in the force predicted by the numerical calculations only appear in the late stages of the loading process, once the deformation is fully localized in the necked sections. The deviation of the force from the fundamental solution occurs slightly earlier as ϖ increases.

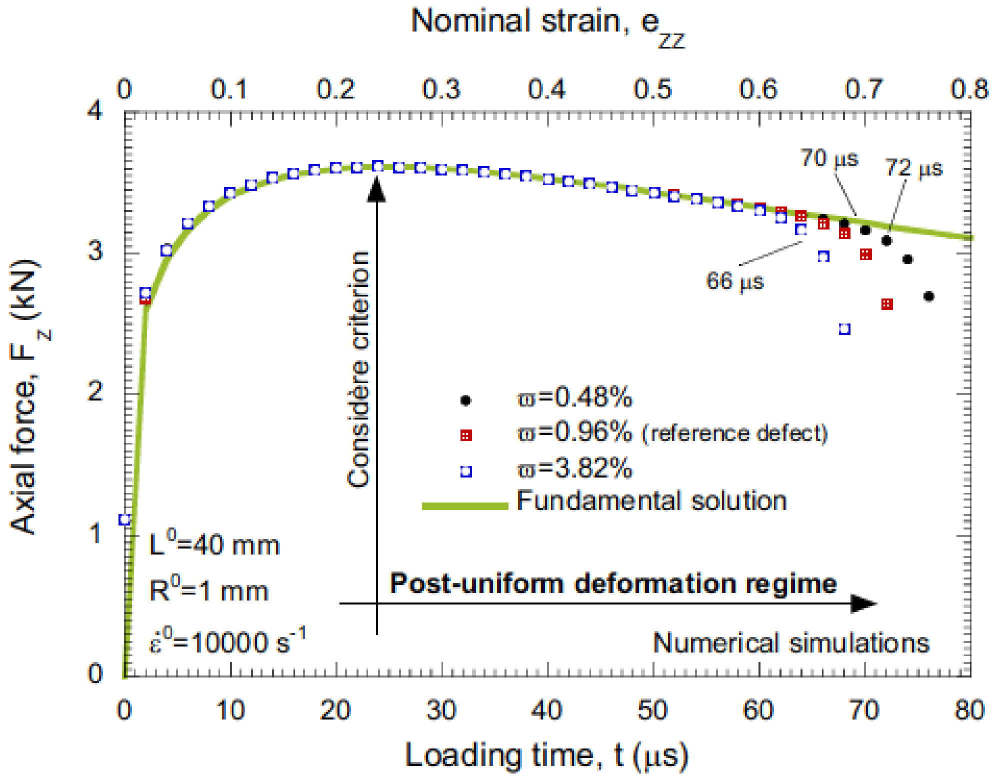

Figure 15: Axial force F_Z versus loading time t and axial nominal strain $e_{ZZ} = \dot{\varepsilon}^0 t$ for the three finite element calculations presented in Fig. 16. The solid green line represents the fundamental solution.

Fig. 16 shows the ratio between the current and the background axial logarithmic strain $\varepsilon_{ZZ}/\varepsilon^b_{ZZ}$ versus the normalized coordinate $\bar{Z}$ for the calculations presented in Fig. 15. Three different loading times are selected: $t = 66\ \mu s$ in Fig. 16(a), $t = 70\ \mu s$ in Fig. 16(b) and $t = 72\ \mu s$ in Fig. 16(c). These loading times, indicated previously in Fig. 15, correspond to the onset of full localization for the three simulations investigated: $\varpi = 3.82\%$, $\varpi = 0.96\%$ (reference case) and $\varpi = 0.48\%$. We observe that as the amplitude of the defect increases, the heterogeneity in the growth rate of the necks during the localization process increases. This suggests that the amplitude of the defect may play a role in the fragmentation process. The necks with greater growth rate will develop into fracture sites, triggering the emergence of unloading waves that could arrest the necks with lower growth rates. Nevertheless, the specific influence of the strain rate defect in the fragmentation process still needs further investigation. However, as anticipated in previous paragraphs, the neck spacing remains independent of ϖ. At $t = 66$ μs the necking pattern in the case of $\varpi = 3.82\%$ is fully developed (the maximum value of the ratio $\varepsilon_{ZZ}/\varepsilon^b_{ZZ}$ is ≈ 2). The necks nucleated close to the ends of the bar have grown faster than those located in the middle of the sample. An important reason for this behaviour is that the defect was near the ends of the specimen (it travelled from the centre of the sample) at the time in which the necking pattern was formed, which led to a greater disturbance of the field variables in those zones of the bar and speeded up the localization process. The necking patterns corresponding to $\varpi = 0.48\%$ and $\varpi = 0.96\%$ are less developed. At $t = 70$ μs only results for $\varpi = 0.48\%$ and $\varpi = 0.96\%$ are shown. Due to the excessive elements distortion inside the necked sections, the calculation for $\varpi = 3.82\%$ stopped before reaching this loading time. The necking pattern in the case of $\varpi = 0.96\%$ is fully developed (the maximum value of the ratio $\varepsilon_{ZZ}/\varepsilon^b_{ZZ}$ is ≈ 2). As previously explained, the growth rate of the necks depends on their location in the bar. Nevertheless, note that the heterogeneity in the rates of growth of the necks is for $\varpi = 0.48\%$ significantly lower than for $\varpi = 0.96\%$. For $t = 72$ μs only results for $\varpi = 0.48\%$ are presented. This is consistent with Fig. 15 where it was shown that the drop of the force corresponding to the full development of the necking pattern occurs slightly earlier as the amplitude of the defect increases. The heterogeneity in the rates of growth of the necks is smaller than in the cases of $\varpi = 0.96\%$ and $\varpi = 3.82\%$. Furthermore, the histogram presented in Fig. 17 shows that the spacing between necks is centred around the average value $\bar{L}^{neck}/\Phi^0 = 1.54$ reported in Fig. 14. The Weibull probability density function given in Eq. (5) has been fitted to the numerical results. The parameters of the distribution, $\chi = 3.176$, $\kappa = 5.895$ and $\lambda = 1.515$, are also similar to those obtained in Fig. 4. Despite the limited number of necks, the Weibull distribution fits the measured neck spacings rather well.

The numerical results presented in this section suggest that, beyond the role played by the defect in the rate of development of the necking pattern, there is a characteristic average neck spacing which, at high strain rates, is controlled to a significant extent by inertia effects. In the next section of the paper we show numerical calculations of samples with various lengths.

6.3. The role of specimen size

We explore the influence of the specimen size on flow localization. Fig. 18 shows the average normalized Lagrangian neck spacing $\bar{L}^{neck}/\Phi^0$ as a function of the initial length of the bar. The values of L^0 investigated range from 5 mm to 300 mm. In any case the initial radius of the

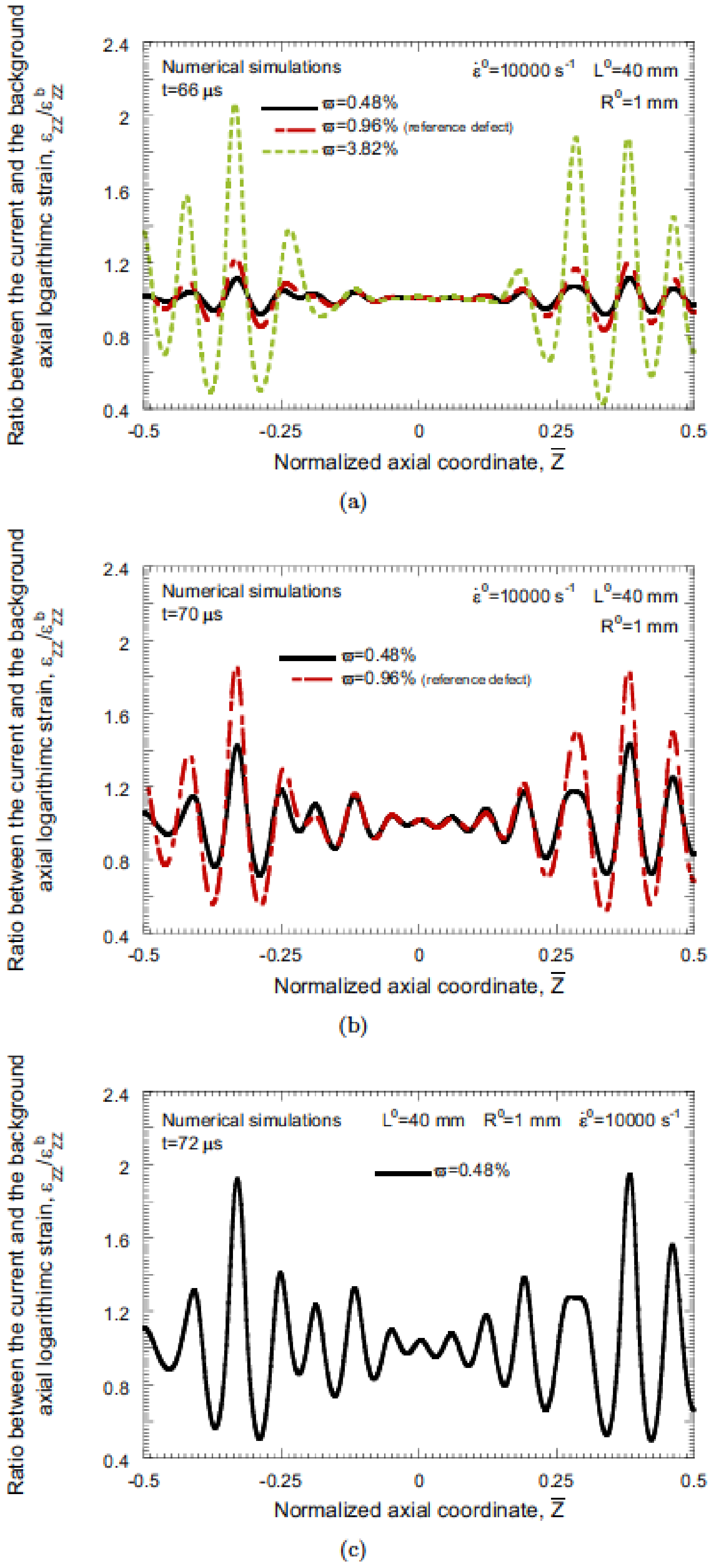

(a)

(b)

(c)

Figure 16: Ratio between the current and the background axial logarithmic strain $\varepsilon_{ZZ}/\varepsilon^b_{ZZ}$ versus the normalized coordinate $\bar{Z} = \frac{Z}{L^0}$. The initial loading rate is $\dot{\varepsilon}^0 = 10000\ s^{-1}$. Results are obtained using finite element calculations for three different strain rate defect amplitudes: $\varpi = 0.48\%$, $\varpi = 0.96\%$ (reference) and $\varpi = 3.82\%$. The defect is included at the center of the specimen. Three different loading times are considered: (a) $t = 66\ \mu s$, (b) $t = 70\ \mu s$ and (c) $t = 72\ \mu s$. The initial length and radius of the bar are $L^0 = 40\ mm$ and $R^0 = 1\ mm$. Due to the excessive elements distortion inside the necked sections, the calculations for $\varpi = 3.82\%$ and $\varpi = 0.96\%$ stopped before reaching $t = 70\ \mu s$ and $t = 72\ \mu s$, respectively, and they could not be shown in subfigures (b) and (c).

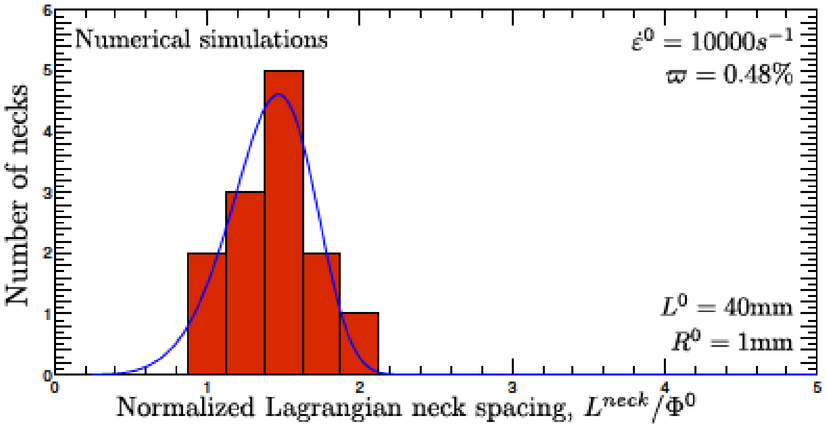

Figure 17: Histogram which presents the number of necks as a function of the normalized Lagrangian neck spacing L^{neck}/Φ^0. The results correspond to the finite element calculation presented in Fig. 16(c). A Weibull probability density function (blue solid line) has been fitted to the numerical results. The parameters of the Weibull distribution are $\chi = 3.176$, $\kappa = 5.895$ and $\lambda = 1.515$.

bar is 1 mm. Three different initial strain rates are considered: $\dot{\varepsilon}^0 = 200\ s^{-1}$, $\dot{\varepsilon}^0 = 2000\ s^{-1}$ and $\dot{\varepsilon}^0 = 10000\ s^{-1}$. Numerical calculations with two different strain rate defect amplitudes are presented: $\varpi = 0\%$ (no defect) and $\varpi = 0.96\%$ (reference defect). Irrespective of the sample length we observe in Fig. 18 that: (1) the influence of the defect in the neck spacing is almost negligible and (2) the neck spacing decreases with the increase of the initial strain rate. These results are consistent with the numerical calculations previously presented in sections 6.1 and 6.2. Moreover, the influence of the sample length in the neck spacing is restricted to short values of L^0, when the number of necks incepted in the bar is lower than 4 or 5. In such a case the average wavelength of the necks seems to be too close to the sample length and the size of the necks becomes affected by the finite dimensions of the rod. Hence, the influence of the length of the bar on $\bar{L}^{neck}/\Phi^0$ is gradually alleviated as $\dot{\varepsilon}^0$ increases since inertia effects reduce the average wavelength of the necks. In fact, for $\dot{\varepsilon}^0 = 10000\ s^{-1}$, the relation between $\bar{L}^{neck}/\Phi^0$ and L^0 is practically an horizontal line (while some disturbances are shown for $\dot{\varepsilon}^0 = 2000\ s^{-1}$). Moreover, note also that, irrespective of the strain rate, the length of the bar used in the calculations presented in sections 5, 6.1 and 6.2 provides neck spacing values virtually independent of L^0. Indeed values larger than 40 mm do not lead to meaningful variations in $\bar{L}^{neck}/\Phi^0$.

Fig 19 shows the axial force F_Z measured at one end of the sample versus the axial nominal strain $e_{ZZ} = \dot{\varepsilon}^0 t$ for three different initial bar lengths: $L^0 = 40\ mm$ (reference case), $L^0 = 120\ mm$ and $L^0 = 260\ mm$. The initial radius of the bar and the initial loading rate are $R^0 = 1\ mm$ and

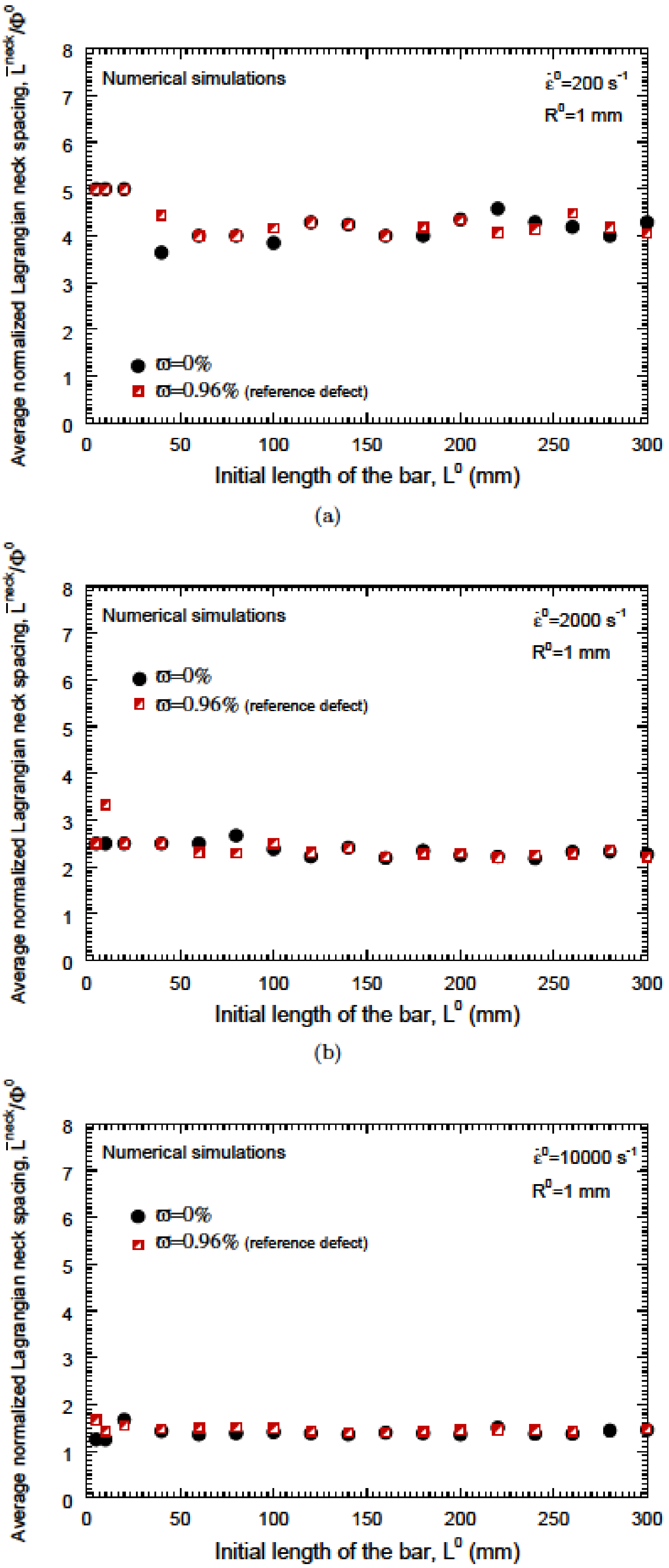

(a)

(b)

(c)

Figure 18: Average normalized Lagrangian neck spacing $\bar{L}^{neck}/\Phi^0$ versus initial length of the bar L^0. Results are obtained using finite element calculations with two different normalized strain rate defect amplitudes: $\varpi = 0$ (no defect) and $\varpi = 0.96$ (reference defect). The defect is included at the center of the specimen. Three initial loading rates are considered: (a) $\dot{\varepsilon}^0 = 200\ s^{-1}$, (b) $\dot{\varepsilon}^0 = 2000\ s^{-1}$ and (c) $\dot{\varepsilon}^0 = 10000\ s^{-1}$. The initial radius of the bar is $R^0 = 1\ mm$.

$\dot{\varepsilon}^0 = 2000\ s^{-1}$, respectively. The force versus longitudinal strain curves for the three bar lengths tested are nearly identical. This reinforces the idea that, for bars longer than 40 mm, the value of L^0 does not affect the mechanical response of the sample. In addition, as mentioned in section 5, we have checked that the force recorded at both ends of the sample is nearly identical.

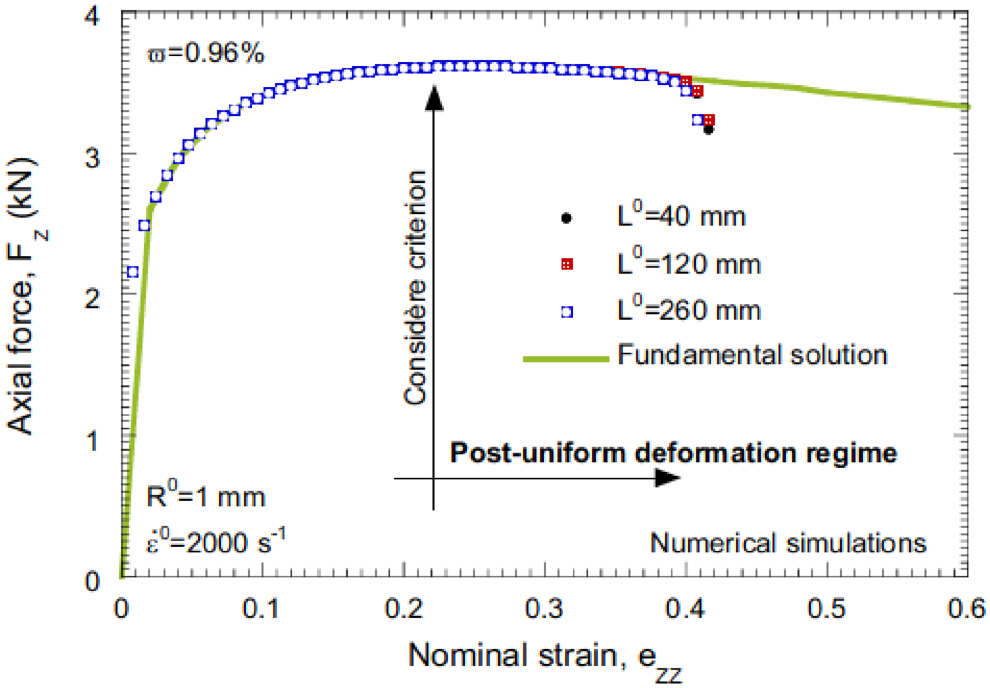

Figure 19: Axial force F_Z versus axial nominal strain $e_{ZZ} = \dot{\varepsilon}^0 t$ for finite element calculations with three different initial lengths of the bar: $L^0 = 40\ mm$ (reference case), $L^0 = 120\ mm$ and $L^0 = 260\ mm$. The initial radius of the bar and the initial loading rate are $R^0 = 1\ mm$ and $\dot{\varepsilon}^0 = 2000\ s^{-1}$, respectively. The defect is included at the center of the specimen. The solid green line represents the fundamental solution.

The histograms presented in Fig. 20 show the number of necks as a function of the normalized Lagrangian neck spacing for the three finite element calculations previously considered in Fig. 19. We observe that, irrespective of the length of the bar, the distance between consecutive necks is centred around the average value $\bar{L}^{neck}/\Phi^0 \approx 2.5$ reported in Fig. 18. The standard deviation of the distribution of neck spacings, which decreases with the bar length, is 0.672 for $L^0 = 40\ mm$ (reference case), 0.515 for $L^0 = 120\ mm$ and 0.467 for $L^0 = 260\ mm$. Thus, as expected, the regularity of the neck spacing increases with the length of the bar. The Weibull probability density function given in Eq. (5) has been fitted to the numerical results. The parameters of the distributions are: $\chi = 1.664$, $\kappa = 8.574$ and $\lambda = 2.451$ for Fig. 20(a), $\chi = 5.845$, $\kappa = 8.965$ and $\lambda = 2.249$ for Fig. 20(b) and $\chi = 12.58$, $\kappa = 6.539$ and $\lambda = 2.342$ for Fig. 20(c). We observe that the fitting is better as the length of the bar, and thus the number of necks, increases.

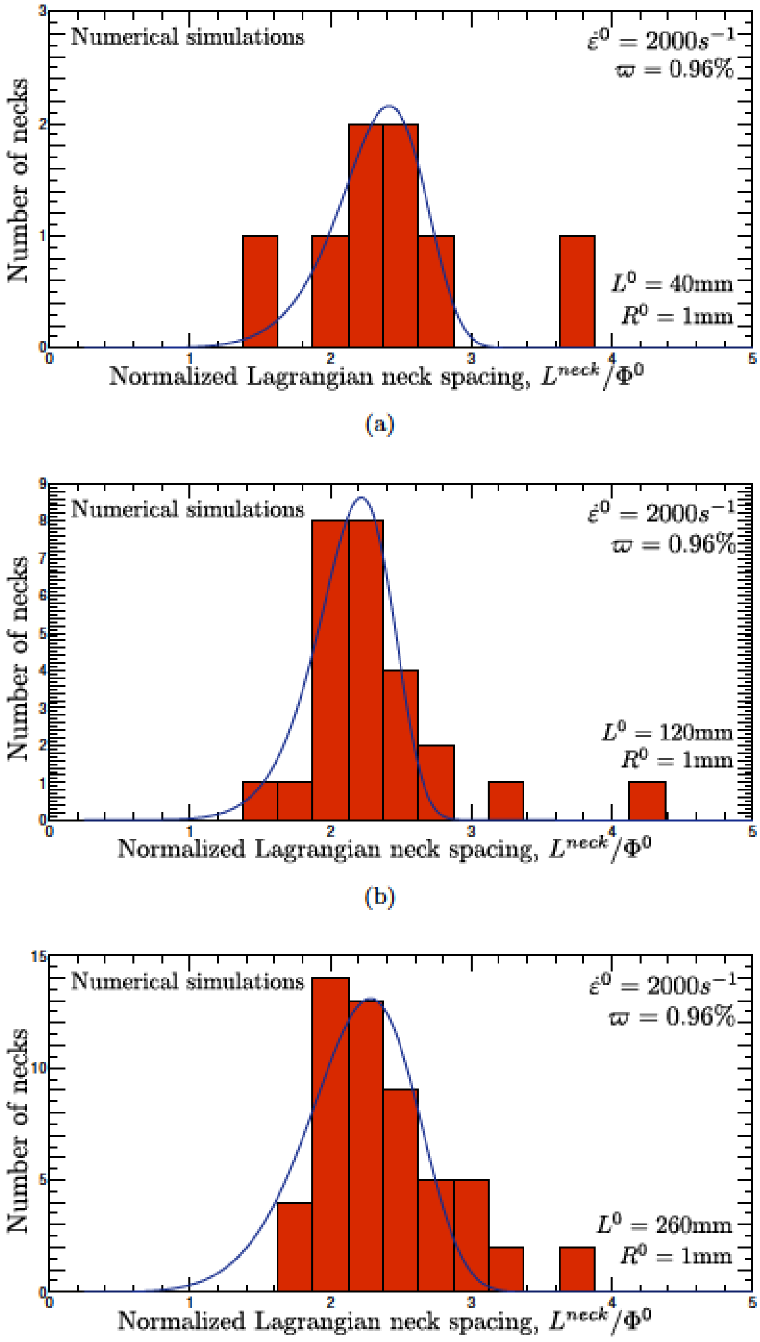

(a)

(b)

(c)

Figure 20: Histograms which present the number of necks as a function of the normalized Lagrangian neck spacing L^{neck}/Φ^0 for finite element calculations with three different initial lengths of the bar: $L^0 = 40\ mm$ (reference case), $L^0 = 120\ mm$ and $L^0 = 260\ mm$. These are the numerical simulations presented in Fig. 19. A Weibull probability density function (blue solid line) has been fitted to the numerical results. The parameters of the Weibull distributions are: $\chi = 1.664$, $\kappa = 8.574$ and $\lambda = 2.451$ for Fig. 20(a), $\chi = 5.845$, $\kappa = 8.965$ and $\lambda = 2.249$ for Fig. 20(b) and $\chi = 12.58$, $\kappa = 6.539$ and $\lambda = 2.342$ for Fig. 20(c).

The calculations presented in this section reveal that the average spacing between necks which characterizes the multiple localization pattern is barely affected by the finite dimensions of the bar. The greater the strain rate, the smaller the average spacing and the smaller the influence of the sample size in the numerical results.

7. Summary and conclusions

In this paper we have demonstrated that the formation of multiple necking patterns in nonlinear incompressible elastic bars subjected to dynamic stretching is largely influenced by inertia effects. For that task we have carried out numerical calculations in ABAQUS/Explicit considering bars of various lengths and subjected to a wide range of strain rates. Moreover, following Ravi-Chandar and Triantafyllidis (2015), we have included in the simulations a strain rate defect. The numerical analysis yielded the following key results:

- The core of the multiple necking process occurs during the post-uniform deformation regime of the bar, at strains larger than the one based on the Considère criterion. It becomes apparent that the existence of a meaningful post-uniform deformation process cannot be disregarded in the analysis of multiple necking at high strain rates. The post-uniform deformation process is greater as the strain rate increases.

- The strain rate defect plays a meaningful role in the rate of growth of the necking pattern during the late stages of the localization process, however it barely affects the average neck spacing. On the one hand, while it is true that this specific issue still requires further analysis, our results suggest that the amplitude of the strain rate defect could play a role in the fragmentation process. On the other hand, the numerical calculations have shown that the number of necks is mostly controlled by the strain rate. Irrespective of the defect amplitude, the number of necks increases with the strain rate.

The results of this paper have been rationalized using 1D and 3D dynamic stability analyses. The agreement between numerical calculations and linear stability analyses is an additional proof of the existence of dominant modes which define, at least up to some extent, the average neck spacing in multiple localization patterns. The specific dominant modes being determined by the emergence of inertia effects at high strain rates. Nevertheless, we acknowledge that this situation may change when considering geometrical or material defects of large(r) amplitude. In such a case, the localization pattern may be dictated by the pre-existing defects up to a certain level of strain rate below which inertia effects are not dominant enough to influence the necking pattern.

Acknowledgements

AVR and JARM are indebted to the *Ministerio de Economía y Competitividad de España* (Projects EUIN2015-62556 and DPI2014-57989-P) for the financial support which permitted to conduct part of this work.

AM and JARM acknowledge the support by the French State through the program Investment in the future operated by the *National Research Agency* (ANR) and referenced by ANR-11-LABX-0008-01 (LabEx DAMAS).

The research leading to these results has received funding from the European Union's Horizon2020 Programme (Excellent Science, Marie Sklodowska-Curie Actions) under REA grant agreement 675602 (Project OUTCOME).

References

Dequiedt, J. L., 2015. Statistics of dynamic fragmentation for a necking instability. International Journal of Solids and Structures 32-44, 107–120.

El Maï, S., Mercier, S., Petit, J., Molinari, A., 2014. An extension of the linear stability analysis for the prediction of multiple necking during dynamic extension of round bar. International Journal of Solids and Structures 51, 3491–3507.

Fressengeas, C., Molinari, A., 1985. Inertia and thermal effects on the localization of plastic flow. Acta Metallurgica 33, 387–396.

Fressengeas, C., Molinari, A., 1994. Fragmentation of rapidly stretching sheets. European Journal of Mechanics A/Solids 13, 251–268.

Grady, D., 1981. Fragmentation of solids under impulsive stress loading. Journal of Geophysical Research 86, 1047–1054.

Grady, D. E., Benson, D. A., 1983. Fragmentation of metal rings by electromagnetic loading. Experimental Mechanics 12, 393–400.

Grady, D. E., Olsen, M. L., 2003. A statistics and energy based theory of dynamic fragmentation. International Journal of Impact Engineering 29, 293–306.

Guduru, P. R., Freund, L. B., 2002. The dynamics of multiple neck formation and fragmentation in high rate extension of ductile materials. International Journal of Solids and Structures 39, 5615–5632.

Hu, X., Daehn, G. S., 1996. Effect of velocity on flow localization in tension. Acta Materialia 44, 1021–1033.

Janiszewski, J., 2012. Ductility of selected metals under electromagnetic ring test loading conditions. International Journal of Solids and Structures 49, 1001–1008.

Kipp, M. E., Grady, D. E., 1985. Dynamic fracture growth and interaction in one dimension. Journal of the Mechanics and Physics of Solids 33, 399–415.

Lindgreen, B., Tvergaard, V., Needleman, A., 2008. Dynamic neck development in a polymer tube under internal pressure. International Journal of Solids and Structures 45, 580–592.

Mercier, S., Granier, N., Molinari, A., Llorca, F., Buy, F., 2010. Multiple necking during the dynamic expansion of hemispherical metallic shells, from experiments to modelling. Journal of the Mechanics and Physics of Solids 58, 955–982.

Mercier, S., Molinari, A., 2003. Predictions of bifurcations and instabilities during dynamic extensions. International Journal of Solids and Structures 40, 1995–2016.

Mercier, S., Molinari, A., 2004. Analysis of multiple necking in rings under rapid radial expansion. International Journal of Impact Engineering 30, 403–419.

Mott, N. F., 1947. Fragmentation of shell cases. In: . Series A. Proceedings of the Royal Society, London, pp. 300–308.

Niordson, F. L., 1965. A unit for testing materials at high strain rates. Experimental Mechanics 5, 29–32.

Petit, J., Jeanclaude, V., Fressengeas, C., 2005. Breakup of copper shaped-charge jets: Experiments, numerical simulations, and analytical modeling. Journal of Applied Physics 98, 123521.

Ravi-Chandar, K., Triantafyllidis, N., 2015. Dynamic stability of a bar under high loading rate: Response to local perturbations. International Journal of Solids and Structures 58, 301–308.

Rodríguez-Martínez, J. A., Molinari, A., Zaera, R., Vadillo, G., Fernández-Sáez, J., 2017. The critical neck spacing in ductile plates subjected to dynamic biaxial loading: On the interplay between loading path and inertia effects. International Journal of Solids and Structures 108, 74–84.

Rodríguez-Martínez, J. A., Vadillo, G., Fernández-Sáez, J., Molinari, A., 2013a. Identification of the critical wavelength responsible for the fragmentation of ductile rings expanding at very high strain rates. Journal of the Mechanics and Physics of Solids 61, 1357–1376.

Rodríguez-Martínez, J. A., Vadillo, G., Zaera, R., Fernández-Sáez, J., 2013b. On the complete extinction of selected imperfection wavelengths in dynamically expanded ductile rings. Mechanics of Materials 60, 107–120.

Rodríguez-Martínez, J. A., Vadillo, G., Zaera, R., Fernández-Sáez, J., Rittel, D., 2015. An analysis of microstructural and thermal softening effects in dynamic necking. Mechanics of Materials 80B, 298–310.

Rusinek, A., Zaera, R., 2007. Finite element simulation of steel ring fragmentation under radial expansion. International Journal of Impact Engineering 34, 799–822.

Vadillo, G., Rodríguez-Martínez, J. A., Fernández-Sáez, J., 2012. On the interplay between strain rate and strain rate sensitivity on flow localization in the dynamic expansion of ductile rings. International Journal of Solids and Structures 49, 481–491.

Xue, Z., Vaziri, A., Hutchinson, J., 2008. Material aspects of dynamic neck retardation. Journal of the Mechanics and Physics of Solids 56, 93–113.

Zaera, R., Rodríguez-Martínez, J. A., Vadillo, G., Fernández-Sáez, J., Molinari, A., 2015. Collective behaviour and spacing of necks in ductile plates subjected to dynamic biaxial loading. Journal of the Mechanics and Physics of Solids. 85, 245–269.

Zhang, H., Ravi-Chandar, K., 2006. On the dynamics of necking and fragmentation - I. Real-time and post-mortem observations in Al 6061-O. International Journal of Fracture 142, 183–217.

Zhang, H., Ravi-Chandar, K., 2010. On the dynamics of localization and fragmentation-IV. Expansion of Al 6061-O tubes. International Journal of Fracture 163, 41–65.

Zhou, F., Molinari, J. F., Ramesh, K. T., 2006. An elasto-visco-plastic analysis of ductile expanding ring. International Journal of Impact Engineering 33, 880–891.